APPLIED SCIENCES AND ENGINEERING

Nano-kirigami with giant optical chirality

Zhiguang Liu[1,4]*, Huifeng Du[2]*, Jiafang Li[1]*†, Ling Lu[1], Zhi-Yuan Li[3]†, Nicholas X. Fang[2]†

Copyright © 2018 The Authors, some rights reserved; exclusive licensee American Association for the Advancement of Science. No claim to original U.S. Government Works. Distributed under a Creative Commons Attribution NonCommercial License 4.0 (CC BY-NC).

Kirigami enables versatile shape transformation from two-dimensional (2D) precursors to 3D architectures with simplified fabrication complexity and unconventional structural geometries. We demonstrate a one-step and on-site nano-kirigami method that avoids the prescribed multistep procedures in traditional mesoscopic kirigami or origami techniques. The nano-kirigami is readily implemented by in situ cutting and buckling a suspended gold film with programmed ion beam irradiation. By using the topography-guided stress equilibrium, rich 3D shape transformation such as buckling, rotation, and twisting of nanostructures is precisely achieved, which can be predicted by our mechanical modeling. Benefiting from the nanoscale 3D twisting features, giant optical chirality is achieved in an intuitively designed 3D pinwheel-like structure, in strong contrast to the achiral 2D precursor without nano-kirigami. The demonstrated nano-kirigami, as well as the exotic 3D nanostructures, could be adopted in broad nanofabrication platforms and could open up new possibilities for the exploration of functional micro-/nanophotonic and mechanical devices.

INTRODUCTION

Three-dimensional (3D) nanofabrication holds the key to building a large variety of micro-/nanostructures with unique and flexible functionalities, compared with their macroscopic counterparts and the 2D planar counterparts, especially in the aspects of integration and reconfiguration. One promising scheme to build 3D micro-/nanostructures is the so-called kirigami or origami method (origami normally refers to the cases when a cutting process is not involved) (*1*, *2*). This method makes use of the art and science of cutting and folding flat objects to create versatile shapes and has been of tremendous interest among both scientists and engineers because of its emerging applications in fields such as micro-/nanoelectromechanical systems (MEMSs/NEMSs) (*3*), energy storage systems (*4*), biomedical devices (*5*), and mechanical and photonic materials (*6*–*9*). Compared with traditional 3D micro-/nanofabrication, kirigami and origami enable the shape transformation from 2D precursors to 3D architectures without the need of precise 3D translation in direct lithography (*10*, *11*) or accurate alignment during indirect multilayer stacking (*12*). Benefiting from their unique transformation characteristics such as rotation and twisting, kirigami and origami greatly enrich the 3D geometries and complexities in the frontier of both fundamental sciences (*2*, *13*) and practical applications (*3*–*5*), compared with those from conventional techniques.

So far, the state-of-the-art kirigami- and origami-based micro-/nanofabrication methods have mainly used the differential strains between neighboring objects to achieve spontaneous curving or folding (*14*–*17*), which can be triggered by stimuli like temperature changes, volume variations, capillary forces, residual removing, etc. For example, one interesting scheme has been recently developed by using the out-of-plane compressive buckling of top precursors induced by an elastomeric support (*17*, *18*). However, most of the schemes were involved with multiple materials or multistep processes that have to be carefully predesigned and strictly sequenced, making it inconvenient for on-site fabrication or flexible addition. Moreover, besides the mechanical characteristics, the unconventional 3D geometries created by kirigami at nanoscale may enable many fascinating properties such as photonic functions at optical wavelengths, which have not aroused sufficient interest. Thus, an instant, high-accuracy, and simple kirigami method, which allows one to reliably generate functional nanogeometries, is highly desirable but has yet to be explored.

Here, we introduce a one-step and on-site nano-kirigami method with nanoscale accuracy by in situ cutting and buckling a suspended gold film. By using the topography-guided stress equilibrium during global ion beam irradiation, versatile buckling, rotation, and twisting of nanostructures are simultaneously or selectively achieved. The exotic 3D structures are accurately controllable by programming ion doses, and well predictable by using an elastoplastic mechanical model. Benefiting from the nanoscale 3D twisting features, giant intrinsic optical chirality is achieved in a 3D pinwheel-like structure, in strong contrast to its 2D counterpart without nano-kirigami. The proposed concept of nano-kirigami, as well as the explored new types of 3D nanostructures, could build up novel platforms for versatile manufacturing techniques and functional structures in areas such as plasmonics, nanophotonics, optomechanics, MEMS/NEMS, etc.

RESULTS

Single-material kirigami

Different from mesoscopic kirigami that usually uses multiple materials, macroscopic kirigami can be simply realized by cutting flat single material and transforming it into desired shapes manually, as the paper-cut of an expandable dome illustrated in Fig. 1A. Single-material kirigami in microscopic scales, which could significantly simplify the multistep processing, is challenging because of the difficulty in finding a sophisticated enough micro-/nanomanipulator. Recent studies found that the local irradiation of thin films with focused ion beam (FIB) could introduce tensile or compressive stress for thin-film folding (*19*–*21*). However, the local irradiation-induced zero curvatures, except at the abruptly folded regions, failed in simultaneous shape transformation of multiple subunits, and were restricted by the overhead beam blocking (fig. S1), which greatly limited the flexibility in structural transformation. Moreover, from the viewpoint of topological classification, these methods belong to the elementary tree–type (open-loop) multibody system (*22*), in which the relative motions within each neighboring object are independent. This is relatively simple compared

[1]Institute of Physics, Beijing National Laboratory for Condensed Matter Physics, Chinese Academy of Sciences, Beijing 100190, China. [2]Department of Mechanical Engineering, Massachusetts Institute of Technology, Cambridge, MA 02139, USA. [3]College of Physics and Optoelectronics, South China University of Technology, Guangzhou 510640, China. [4]University of Chinese Academy of Sciences, Beijing 100049, China.
*These authors contributed equally to this work.
†Corresponding author. Email: jiafangli@aphy.iphy.ac.cn (J.L.); phzyli@scut.edu.cn (Z.-Y.L.); nicfang@mit.edu (N.X.F.)

Downloaded from http://advances.sciencemag.org/ on July 6, 2018

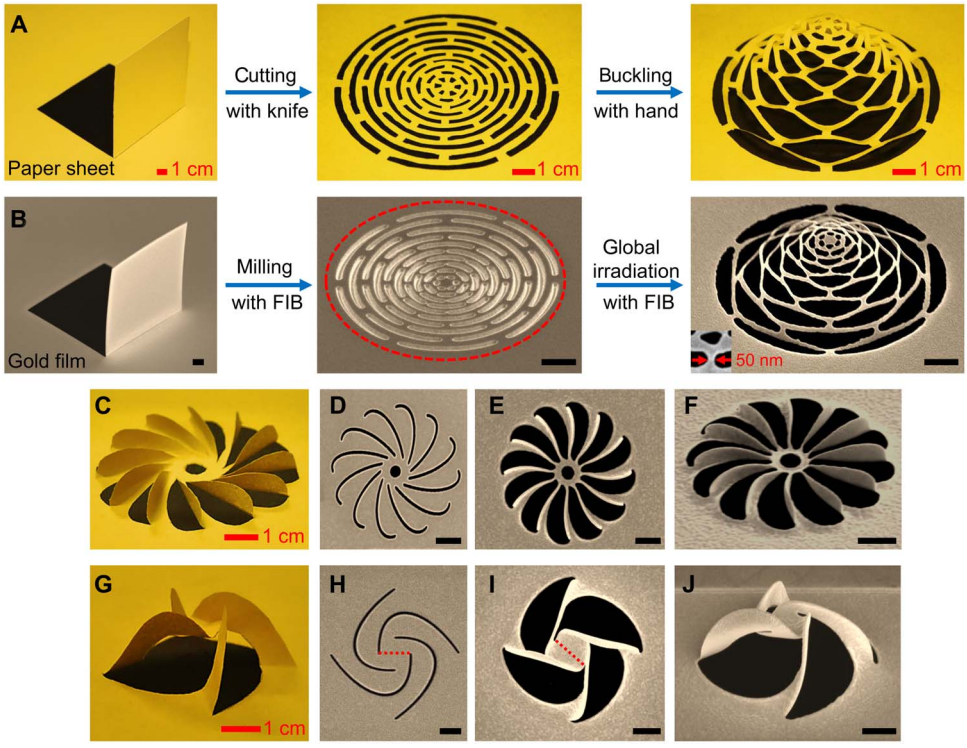

Fig. 1. Macro-kirigami and nano-kirigami. (**A**) Camera images of the paper kirigami process of an expandable dome (corresponding to a traditional Chinese kirigami named "pulling flower"). (**B**) SEM images of an 80-nm-thick gold film, a 2D concentric arc pattern and a 3D microdome. The high-dose FIB milling corresponds to the "cutting" process, and the global low-dose FIB irradiation of the sample area (enclosed by the dashed ellipse) corresponds to the "buckling" process in nano-kirigami. The buckling direction is downward along the FIB incident direction (fig. S1G). A 3D feature size of 50 nm is shown in the inset. (**C** to **F**) A 12-blade propeller and (**G** to **J**) a four-arm pinwheel formed in a macroscopic paper and a gold nanofilm, respectively. Top-view SEM images of the milled 2D patterns before (D and H) and after (E and I) global FIB irradiation from the top, respectively. (F) and (J) are the side views of (E) and (I), respectively, which are in good correspondence to the macro-kirigami in (C) and (G). The dashed lines in (H) and (I) indicate a connection between two corners of the central structure, revealing a rotation angle of ~41° by nano-kirigami. The in situ fabrication can be programmed into one step (movie S1). Scale bars in SEM images, 1 μm.

to the advanced kirigami in close-loop multibody systems (*22*), in which the relative motions within the loop become dependent; that is, a relative motion of one object affects the relative motions of the others. Actually, the interrelated shape transformation of neighboring bodies represents one of the most intrinsic natures of kirigami and provides an extra freedom toward 4D manufacturing (*23*), which is highly desirable but has not been implemented in nanometer accuracy with desirable functionality.

Our nano-kirigami method exhibits the features of close-loop multibody systems; that is, the final formation of the interconnected structures is determined by the overall stress equilibrium other than the isolated folding of individual components. As shown in Fig. 1B, through high-dose milling and low-dose global irradiation with gallium ion–based FIB, the paper-cut of the expandable dome is well reproduced in microscopic scale, with sub–50-nm feature size in an 80-nm-thick gold film (see Materials and Methods). This is a "buckling down" process since the rising direction of the nanostructures is along the illumination direction of the ion beam (movie S1 and fig. S1G). In more general topographic designs, 2D patterns are found to be much easier to buckle up (inverse to the ion beam illumination direction), as shown by the 12-blade propeller in Fig. 1 (C to F) and the four-arm pinwheel in Fig. 1 (G to J). It is observed that the central part of the structure can be dynamically twisted and rotated during the buckling up process, as illustrated by the rotated dashed lines in Fig. 1 (H and I), exhibiting a typical signature of the close-loop multibody systems that cannot be achieved with tree-type fabrication methods. Moreover, all these complex structures (including other 3D structures in the following contents and in fig. S2) could be readily realized by programming the irradiation dose in one step or instantly adding in flexible orders (movie S1 and fig. S1G), which are challenging for traditional 3D fabrication methods and for the prescribed tree-type kirigami and origami methods.

Topography-guided nano-kirigami

The main mechanism of the nano-kirigami is to use the residual stress induced by the gallium ion collisions with gold thin films (*20*, *21*, *24*), as illustrated in Fig. 2A. Specifically, when the sample area is exposed to ion irradiation, some of the gold atoms are sputtered away from the surface and the resulting vacancies cause grain coalescence (*24*, *25*), which induces tensile stress close to the film surface. Meanwhile, some gallium ions are implanted into the film, which induces compressive stress. The two stresses occur simultaneously within ~20 nm of the gold film (fig. S3), and the combination of them determines the overall stress within the ion beam–affected top layer, which deforms the less-affected bottom layer of gold. Our tests show that tensile stress is dominant when FIB with acceleration voltage of 30 kV is applied to a 80-nm-thick gold film (fig. S4). Therefore, the free-standing gold film in our case could be simplified into a bilayer model; that is, the top amorphous layer with tensile stress σ_t and the bottom layer with deformation stress σ_b. In such a model, when one end of the suspended structure is fixed, the top

Downloaded from http://advances.sciencemag.org/ on July 6, 2018

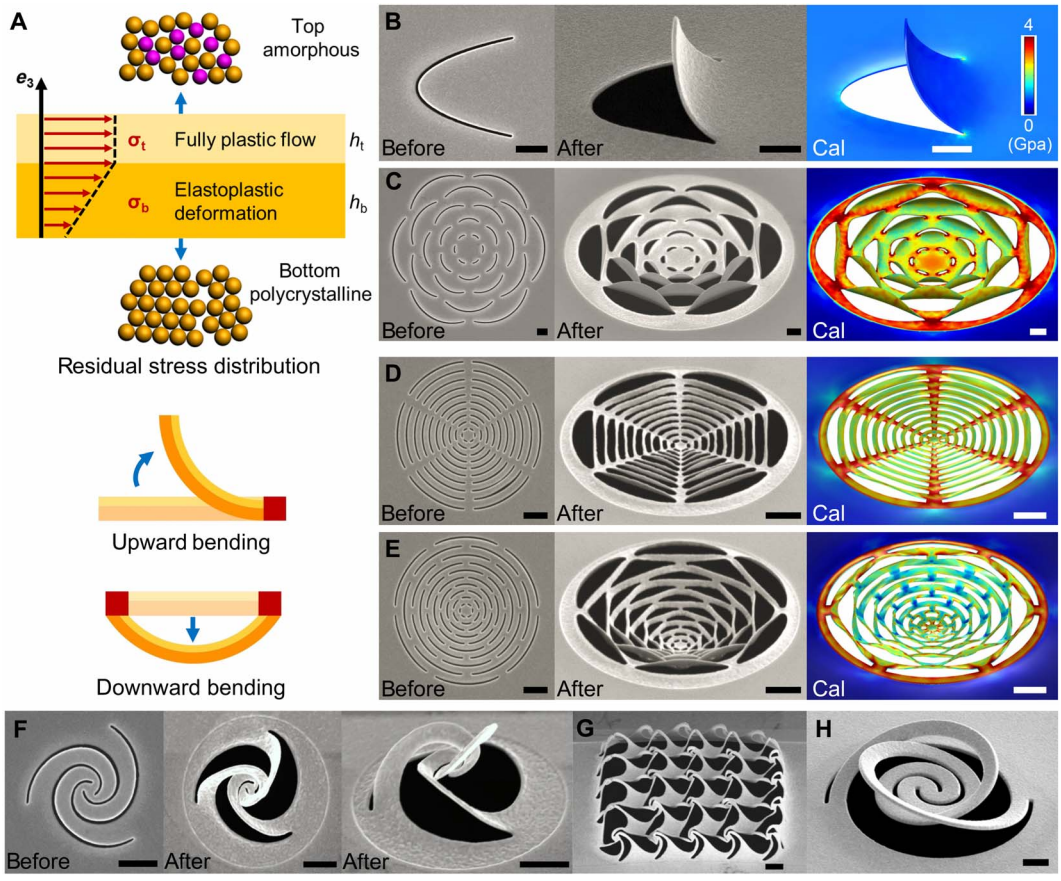

Fig. 2. Topography-guided nano-kirigami. (**A**) Schematic illustration of residual stress distribution of gold nanofilm under global ion beam irradiation. In this bilayer model (section S1), the constant tensile stress (σ_t) is dominant within the top amorphous layer, and the elastic stress (σ_b) is linearly distributed across the bottom polycrystalline layer. In such a case, when one edge is fixed (as noted by the red squares), the cantilever will bend upward. While both boundaries of the cantilever are fixed, the film could bend downward under the topography-guided stress equilibrium. (**B** and **C**) SEM images of (B) a tongue-like structure and (C) a flower-like structure before and after global ion beam irradiation. The calculated (Cal) structures well represent the upward bending process. (**D** and **E**) SEM images of (D) a spider web–like and (E) a concentric arc structure before and after global ion beam irradiation, showing distinctive downward buckling amplitudes under the same irradiation. (**F** to **H**) SEM images of (F) a twisted triple Fibonacci spiral, (G) window decoration–type nanobarriers, and (H) a deformable spiral. Calculated results in (B) to (E) are displayed with the same color bar as in (B). Scale bars, 1 μm.

tensile stress will cause the suspended structure to bend upward, like the scanning electron microscopy (SEM) images of tongue-like bending shown in Fig. 2B. This upward bending mechanism can be simultaneously applied to the multiple subunits of complex geometries, such as the upward bent "petals" of the flower-like structure in Fig. 2C (movie S2).

The precise modeling of nano-kirigami process is of critical importance since it is able to help one predict and visualize the final form of the structures. However, this is challenging in nanoscale, since the FIB-induced structural changes and material modifications are usually beyond the elastic region, and previous assumptions of purely elastic material dealing with Stoney formula are inadequate for complex structural transformation (*24*). We hereby develop a comprehensive mechanics model in which constant tensile stress (σ_t) dominates the top amorphous layer because of the presence of plastic flow, and the bottom layer has a linear distribution of elastic stress (σ_b) as a consequence of bending deformation induced by contraction of the top layer (section S1), as illustrated in Fig. 2A. In such a case, the residual stress will cause the structure to bend globally under the guidance of the initial topographies until new equilibrium morphologies are reached. Considering the ultrasmall film thickness (50 to 80 nm), the residual stress distribution in our mechanical model could be simplified by (section S1)

$$\sigma^{\text{in-plane}}(x_3) = \begin{cases} \sigma_t = \text{const}, & h_b < x_3 \le h_b + h_t \\ \sigma_b = \sigma_0^{\text{in-plane}} + kx_3 + o(x_3), & 0 \le x_3 \le h_b \end{cases} \quad (1)$$

Here, x_3 is the coordinate in the thickness direction (e_3); h_t and h_b are the thicknesses of top and bottom layers, respectively; σ_t and σ_b are the residual stress in the top and bottom layers, respectively; $\sigma_0^{\text{in-plane}}$ and k are the first- and second-order coefficient in the asymptotic expansion of stress in the bottom layer, with little $o(x_3)$ representing the higher orders (the higher-order term is negligible considering the ultrasmall thickness of the films). With such a residual stress distribution, the fabricated structures are well reproduced by the numerical calculations, as shown in Fig. 2 (B and C), verifying the accuracy of our model.

The topography of the 2D patterns is crucial in our nano-kirigami; that is, the structural bending direction can be varied by modifying the boundaries of the 2D patterns. As illustrated in Fig. 2A, when the

Downloaded from http://advances.sciencemag.org/ on July 6, 2018

boundaries of the ion beam irradiation area are changed, for example, when the multiple ends of the suspended area are fixed, the structures could possibly be buckled in a downward direction under the same residual stress. As shown in Fig. 2 (D and E), by changing the arc length and its filling ratios, the arc patterns are buckled downward after global ion beam illumination, entirely different from the upward bent petals in Fig. 2C (movie S2). Even for arc structures with the same aspect ratio and arc length, the downward buckling of the concentric arc structure in Fig. 2E is significantly larger than that of the spider web pattern in Fig. 2D (~240% larger in the calculation of fig. S6). These observations are well reproduced by the calculations in Fig. 2 (C to E) under the same stress σ_t and σ_b. The accurate modeling provides more information beyond the structural configurations, such as the final distribution of equilibrium stresses under distinctive topographies. For example, for the spider web structure in Fig. 2D, the calculated stress is mainly concentrated on the radial connection parts (*26*), while the concentric arc structure in Fig. 2E shows relatively uniform stress distribution. Therefore, under the same aspect ratio, the spider web structure is more fragile than the concentric arc structure when a large dose of ion beam irradiation is applied (verified in fig. S6C and movie S3). The excellent consistence between experiments and calculations proves that, in the proposed nano-kirigami, the shape transformation among neighboring parts is strongly interrelated through the stress equilibrium among multiple branches, and the resulting structures are well predictable by the mechanical model. Following this design principle, a wide range of complex 3D derivatives (fig. S2) is generated with the nano-kirigami method, such as the twisted Fibonacci spirals (Fig. 2F), the window decoration–type interconnected nanobarriers (Fig. 2G), and potentially deformable MEMS spirals (Fig. 2H) (*27*). These 3D exotic nanostructures have not been seen with the conventional nanofabrication techniques and may largely enrich the variety of nanophotonic devices and MEMS/NEMS in both designs and fabrications.

Functional designs for optical chirality

While the applications of mesoscopic kirigami and origami techniques are mainly in mechanical or acoustic areas, the versatile geometries introduced by nano-kirigami open a door for nanophotonic applications. For example, from the photonic point of view, the out-of-plane twisting by nano-kirigami could help to facilitate unique electromagnetic properties such as 3D optical chirality. It is well known that intrinsic chirality, the geometric property of a structure lacking any mirror symmetry plane, exists only in 3D, and its optical response could be several orders of magnitudes higher in artificial nanostructures than that in natural chiral materials (*28*–*31*). While extrinsic optical chirality has been observed in planar 2D structures (*29*, *32*), it typically requires strict oblique incidence, and the chiral responses are relatively weak. This is because the physical origin of the optical chirality comes from the cross-coupling between the electric and the magnetic dipoles in parallel directions (*33*). In the case of normal incidence, the induced magnetic dipoles in 2D structures are along the incident direction and, thus, perpendicular to the direction of electric dipoles, which makes them uncoupled and results in the lack of chirality. Therefore, 3D structures with twisting features in the propagation direction such as vertical helices (Fig. 3A) are highly desirable to realize strong optical chirality (*10*). However, to operate at optical or telecommunication wavelength region, the twisting elements have to be miniaturized to submicrometer scales, which is challenging because of the fabrication restrictions and, thus, limited to a few specialized techniques (*34*, *35*). Thus, a simple 3D nanofabrication approach, with a high degree of freedom and capable of generating nanoscale twisting elements, is appealing.

Considering the exotic geometries by nano-kirigami, the design of 3D chiroptical nanostructures could be intuitively extended by rotating the vertical helices to form horizontal cross-linked helices and further evolved into a fully metallic pinwheel array, as illustrated in Fig. 3A, of which the fabrication restrictions can be readily solved by nano-kirigami (as in next paragraph). Because of the twisted loops in all directions (*28*), the electric field (E_x) of the incident light could induce both electric ($p_{x,L}$) and magnetic ($m_{x,L}$) moments in the parallel direction (that is, $p_{x,L}//m_{x,L}//x$) for the left-handed (LH) pinwheel, as illustrated in Fig. 3B. In the same manner, the electric ($p_{y,L}$) and magnetic moments ($m_{y,L}$) along y direction could also be induced by the magnetic field (H_y) of the incident light (Fig. 3C). Since optical chirality is dependent on the strength of $p \cdot m$ (*36*), the parallel electric and magnetic moments can interact strongly to induce pronounced optical chirality. Meanwhile, it can be seen that the direction of the induced electric and magnetic moments is highly dependent on the LH or right-handed (RH) twisting of the four arms. Specifically, in the LH pinwheel, the direction of $p_{x,L}$ and $p_{y,L}$ is opposite to that of $m_{x,L}$ and $m_{y,L}$, respectively, which causes an LH chiroptical response (*9*, *28*). In comparison, the direction of $p_{x,R}$ and $p_{y,R}$ is the same as that of $m_{x,R}$ and $m_{y,R}$, respectively, revealing that the RH windmill has an RH chiral response.

To take advantage of the nano-kirigami, we intuitively designed three types of 2D spiral patterns, as shown in Fig. 3D. After applying the same residual stress with our mechanical model, 3D pinwheel structures with different height and arm width are predicted, as shown in Fig. 3D, which are geometrically equivalent to the pinwheel design in Fig. 3A. These numerical designs and results are well verified by the fabricated structures in Fig. 3E, revealing the accuracy and robustness of the proposed mechanical models. It can be seen from the SEM images that the top ends of the arms in type I pinwheel and the bottom ends of the arms in type III pinwheel are very thin. In comparison, the type II 3D pinwheel has more uniform arms, which are more stable when the structures are further scaled down (fig. S8). Therefore, to achieve desirable optical chirality with high structural stability, type II design will be used in the following studies (movie S4).

Giant optical chirality in exotic 3D nanostructures

To realize optical chirality in telecommunication wavelengths, 2D and 3D pinwheel arrays with lattice periodicity of 1.45 μm are successfully fabricated, as shown in Fig. 4 (A and B), where the 3D twisted arms are identified after the global ion beam illumination of the 2D patterns. It should be mentioned that, when the arm width of the pinwheel reaches around ~100 nm, the dislocation and diffusion of the gold atoms (*37*) under global ion irradiation start to affect the morphology of the structures. As a result, the arms of the pinwheel in Fig. 4B become relatively round compared with the twisted flat arms in Fig. 3E.

Optical chirality of these structures can be characterized by $\chi = (n_R - n_L)/2$, where n_R or n_L is the effective refractive index of the RH or LH circularly polarized (RCP or LCP) light. The real part of χ causes different phase delays for RCP and LCP light and is represented by circular birefringence that results in the rotation of the linear polarization by an angle $\theta = (n_R - n_L)\pi d/\lambda_0$, where d is the thickness of the chiral medium, and λ_0 is the light wavelength in vacuum (*29*). The imaginary part of χ corresponds to circular dichroism (CD), which causes different absorption losses for RCP and LCP waves.

Optical measurements show that the 2D structure in Fig. 4A does not have any CD and circular birefringence effect under normal incidence (Fig. 4, D and E), as expected because of its 2D nature. In comparison, the experimental 3D pinwheel structure in Fig. 4 (B and C)

Downloaded from http://advances.sciencemag.org/ on July 6, 2018

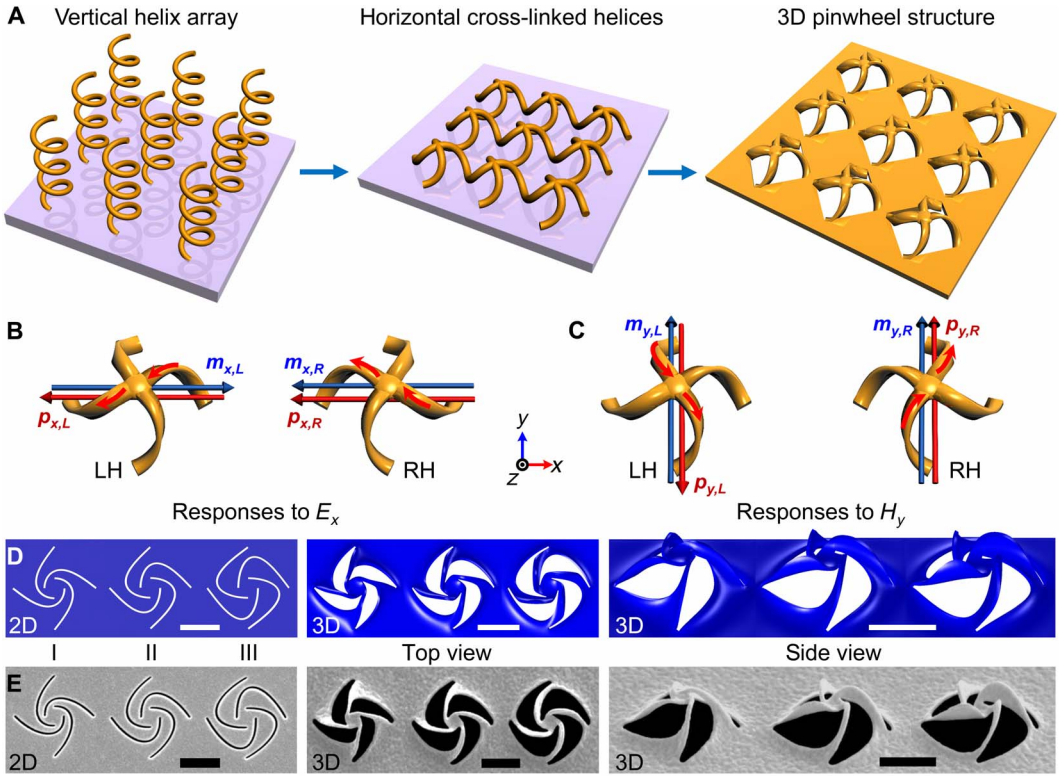

Fig. 3. Functional designs for optical chirality. (**A**) Schematic of vertical helix array, horizontal cross-linked helices, and a 3D pinwheel array [the 3D pinwheel can also be treated as two cross-linked and twisted ohm-shaped circuits (*28*) standing onto a metallic hole array]. (**B** and **C**) Illustration of the responses to the (B) electric field (E_x) and (C) magnetic field (H_y) of incident light for the LH and RH twisted pinwheels, respectively. The direction of induced electric moments $p_{i,j}$ ($i = x$ or y, $j = L$ or R) and magnetic moments $m_{i,j}$ at the center parts is noted by the arrows for LH ($j = L$) and RH ($j = R$) pinwheels, respectively (generalized from the simulated results in fig. S7). (**D**) Numerical designs of three 2D spiral patterns (types I, II, and III), the top view, and side view of the numerically predicted 3D structures, respectively, under the same residual stress distribution. (**E**) SEM images of the fabricated 2D patterns and corresponding 3D pinwheels after global ion irradiation with the same doses, agreeing excellently with the numerical predictions. Scale bars, 1 μm.

exhibits clear CD effects, in which the CD spectra of LH and RH 3D structures show nearly opposite signs with similar amplitudes, as the curves plotted in Fig. 4D. This is in good agreement with the analysis in Fig. 3 (B and C). Meanwhile, pronounced circular birefringence versus wavelength is observed, as plotted in Fig. 4 (E and F), in which the rotation angle (θ) of the linear polarization increases markedly in the long wavelength region. The polarization rotation angles reach ~90° and ~135° at 1.70 and 1.95 μm, respectively, without making the polarization state elliptical (Fig. 4F). Considering the overall structural thickness of ~430 nm (including the bottom layer), such circular birefringence is giant compared to the statistics of chiral metamaterials and planar structures in the literature (*36*). The experimental results agree well with the calculations and unambiguously show that, by simply introducing 3D twisting structures through nano-kirigami, the optical chirality can be significantly enhanced compared with that of the 2D counterpart. Meanwhile, it shows that compared to other chiral structures with multilayer or twisting designs in terahertz, gigahertz, or mid-infrared wavelengths, the nano-kirigami has nanoscale accuracy while markedly simplifying the fabrication difficulty without reducing the structural complexity (*33*).

DISCUSSION

We have demonstrated a novel 3D nanofabrication technology based on an on-site nano-kirigami method that is applicable by programming the dosages of the ion beam irradiation in one step. On the basis of the deliberate engineering of the topography-guided stress equilibrium of gold nanostructures during ion beam irradiation, versatile 3D shape transformations of nanoscale structures were simultaneously and selectively achieved. Compared with traditional 3D nanofabrication techniques such as direct writing (*10*) and multilayer stacking (*12*), the nano-kirigami method significantly simplifies the fabrication complexity while retaining the diversity and functionality of 3D nanostructures. Meanwhile, it overcomes the prescribed and multistep procedures in traditional mesoscopic kirigami and origami methods by instantly cutting and buckling nanofilms with the same ion beams, which makes it convenient to perform nanometer-accurate kirigami in one step. The exotic 3D structures have been well predicted by using an elastoplastic mechanical model, which not only provides a reliable tool for feasibility tests and internal stress analysis but also opens a window for inverse designs of desirable functionalities. Finally, as a functionalization of the nanoscale 3D twisting features, an exotic gold pinwheel with giant optical chirality has been realized in telecommunication wavelengths. Since the 3D pinwheels have fourfold (C4) rotational symmetry on the *z* axis, the chirality is expected as uniaxial for normal incident light (*28*). The strong chiroptical responses were not observed in the corresponding 2D counterpart, unambiguously revealing the significance brought by the nano-kirigami. It should be noted that if the C4 pinwheels are arranged in triangular lattices with sixfold rotational (C6) lattice symmetry, then the resulting 3D structures will have twofold rotational (C2) symmetry. In such a case, circular polarization conversion can be observed

Downloaded from http://advances.sciencemag.org/ on July 6, 2018

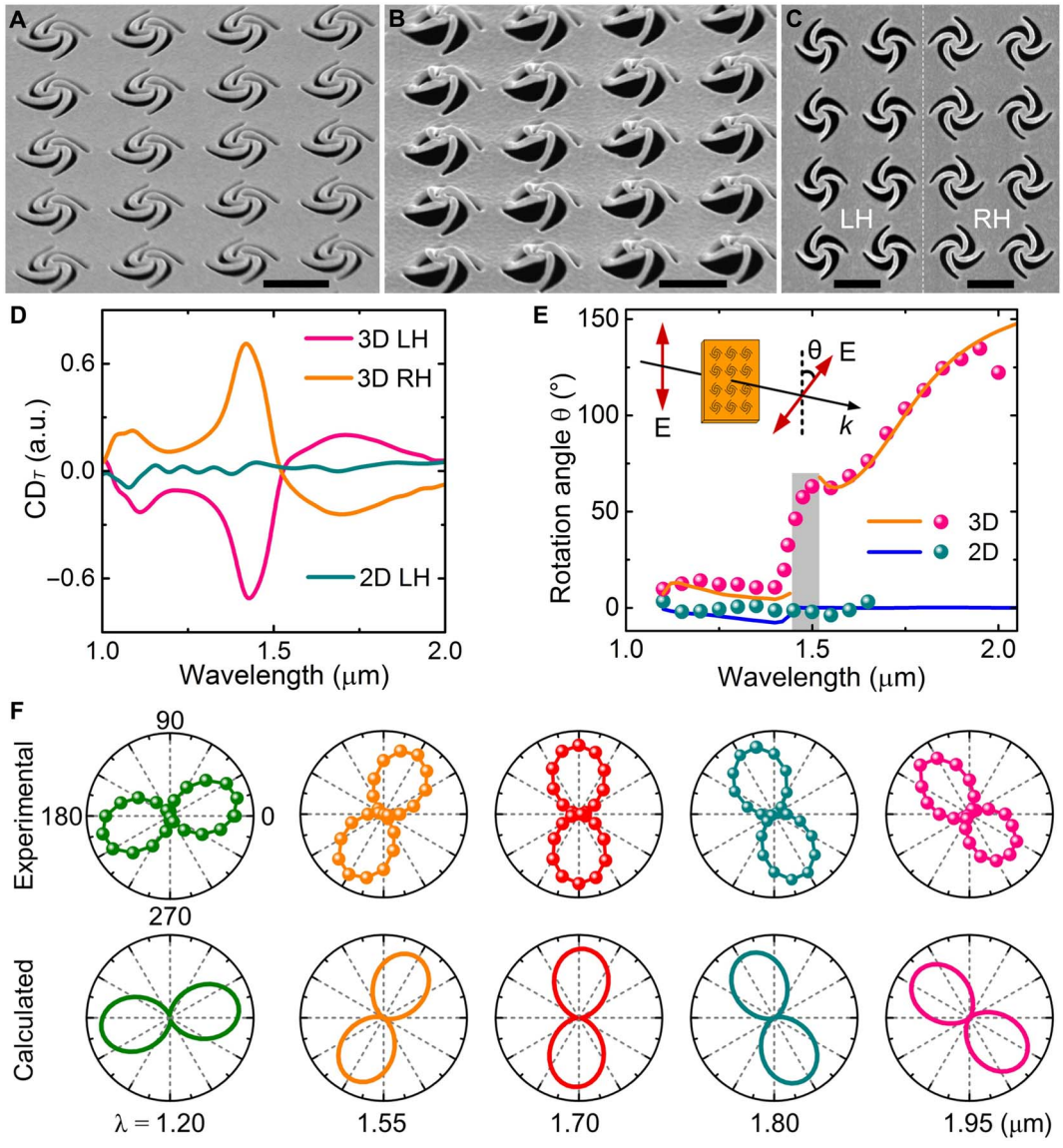

Fig. 4. Giant optical chirality. (**A** and **B**) SEM images of (A) 2D and (B) 3D pinwheel array with periodicity of 1.45 μm. The height of the 3D pinwheels is about 380 nm. (**C**) Top-view SEM images of LH and RH 3D pinwheel arrays. Scale bars, 1 μm. (**D**) Measured CD in transmission [defined as $CD_T = (T_L - T_R)/(T_L + T_R)$] versus wavelength for 2D LH, 3D LH, and 3D RH pinwheels, respectively. a.u., arbitrary units. (**E**) Measured (circular points) and calculated (solid lines) linear polarization rotation angle (θ) versus wavelength for 3D and 2D LH pinwheels, respectively. The unrealistic abrupt peaks around 1.45 μm in calculation are not shown for clearance because of the inaccurate retrieval of polarization states at nearly zero transmission at Wood's anomaly (see full calculated data in fig. S9). Inset: Schematic of the linear polarization rotation. (**F**) Polar plot of (top) experimental and (bottom) calculated transmission versus detection polarization angle at specific wavelengths under *x*-polarized incidence for the 3D LH pinwheels. Nearly linearly polarized states are observed. In comparison, for wavelengths in the strong CD region (around 1.45 μm), the measured transmission of light exhibits elliptical polarization states (fig. S9H). Spectra are measured from 1.1 to 2 μm because of the restriction of the quarter-wave plate (see Materials and Methods).

at a certain wavelength region. The studies in this aspect are interesting and deserve profound investigation.

One distinctive feature of our nano-kirigami method is that, during the global ion beam irradiation, the thinning and transformation of nanofilm, accompanied by the atom dislocations and diffusions, occur simultaneously across the whole sample region other than localized at the sequential folding areas. Therefore, the topography-guided stress equilibrium among subunits, instead of individual folding, determines the final structural configuration. Compared to the FIB-induced deposition method (*38*, *39*), this proof-of-concept nanofabrication could be applied to a wide variety of suspended thin-film materials [such as aluminum and commercial silicon nitride thin films in fig. S10 (A and B)] and to other ion-based etching or implant systems to achieve large-scale fabrications, although the specific stress responses may be different from those of gold (section S3). The geometries of the enabled 3D structures could also be extended to other types, such as three-arm 3D pinwheels that break the center-inversion symmetry (fig. S10, C and D). Moreover, the suspending features endow the 3D nanostructures with potential applications on reconfigurable nanophotonic and optomechanical devices by engineering the suspended subunits, such as

Downloaded from http://advances.sciencemag.org/ on July 6, 2018

the scheme used by commercial digital micromirror devices in digital light processing projection and related 3D printing industry. Therefore, our work here not only builds up a new nanofabrication concept and platform for diverse structural geometries and functionalities but also opens up new possibilities for the active configuration of versatile micro-/nanophotonic and electronic devices.

MATERIALS AND METHODS

Numerical simulations

The transmission spectra and electromagnetic field distributions of the 2D and 3D gold structures were simulated by using the finite element method. The current distributions were obtained by using a current density monitor in commercial software package CST Microwave Studio based on the finite integration method. Periodic boundary conditions along the *x*- and *y*-axis direction were applied to the unit cell of the simulated structures. Incident plane wave was incident along the *z*-axis direction, which was identical to the conditions in experiments. The refractive index and extinction coefficient of gold were described by the Lorentz-Drude model. The thickness of the target nanostructures after nano-kirigami transformation was set to 50 nm in simulations unless otherwise specified, which was under the consideration of the sputtering effect during the global ion beam irradiation and confirmed in SEM characterizations. The deformed configurations of 3D nano-kirigami architectures were calculated with finite element software SIMULIA Abaqus FEA and COMSOL Multiphysics. User-defined subroutines were implemented for applying the nonuniform residual stress field to trigger global buckling of nanofilms. More details related to modeling can be found in sections S1 and S2.

Sample fabrications

All the 3D structures were fabricated with a dual-beam FIB/SEM system (FEI Helios 600i) on self-supporting gold nanofilms. The 80-nm-thick gold film suspended on copper grid was prepared by lift-off process in previous studies and directly used here (*40*). To avoid unwanted film fluctuations, multiple flat and clean sample areas satisfying the fabrication requirements were carefully selected from more than 100 meshes on the copper grid. The maximum size of each sample area is ~100 μm × 100 μm, which is limited by the mesh size. For large-scale fabrication, suspended nanofilms with desirable flatness are commercially available, such as the silicon nitride film window (500 μm × 500 μm × 50 nm in size; Norcada) used in fig. S10B. The nano-kirigami method includes a two-dosage ion beam irradiation. First, the 2D patterns were directly cut by the FIB under high doses of 1.9×10^8 ions/μm (>600 pC/μm^2). Subsequently, global ion beam irradiation was conducted by frame-scanning the effective sample area with relative low doses of 10 to 40 pC/μm^2 without particular alignment. The whole process could be programmed into one step and in situ monitored by the SEM (see movie S1). The acceleration voltage and current beam of Ga^+ were set at 30 kV and 24 pA, respectively, if not mentioned. In such a case, the nano-kirigami took a few minutes for most of the single structures. For an array of 3D pinwheels with lattice period of 1.45 μm and sample area of 30 μm × 30 μm, the fabrication time was less than 30 min. Because of the large scales of the structure, the overall fabrication resolution was about 20 nm.

Optical characterizations

The optical measurements were performed using a homemade spectroscopy system designed to characterize samples with small sizes. For transmission spectral measurement, white light from tungsten halogen source (HL-2000, Ocean Optics) or supercontinuum light sources (SC400-4, Fianium) was collimated and confined to proper beam size, which was then weakly focused onto the sample by a near-infrared (NIR) objective lens [×10, 0.25 numerical aperture (NA); Olympus]. The transmitted signals were collected using another NIR objective lens (×100, NA 0.9; Olympus) and delivered to a spectrometer (SP-2300, Princeton Instruments) equipped with a liquid nitrogen–cooled charge-coupled device (CCD) detector (PyLoN-IR). An NIR CCD camera (XS-4406, Xenics) was set within the switching optical path for imaging. For measurement of CD, a linear polarizer (650 to 2000 nm; Thorlabs) and a quarter-wave plate (1100 to 2000 nm; Thorlabs) were inserted into the input optical path at specific orientations. Therefore, the spectra in this work were mainly focused on wavelength range from 1100 to 2000 nm. Linear polarization rotation experiments were conducted by varying the detection polarization (linear polarizer, 650 to 2000 nm; Thorlabs) at every 15° under linearly polarized incidence.

SUPPLEMENTARY MATERIALS

Supplementary material for this article is available at http://advances.sciencemag.org/cgi/content/full/4/7/eaat4436/DC1

Section S1. Mechanical modeling
Section S2. Optical modeling
Section S3. Extension of nano-kirigami to other materials and geometries
Fig. S1. Illustration of the overhead ion beam blocking and comparison between local and global ion beam irradiation.
Fig. S2. Exotic 3D structures fabricated by nano-kirigami.
Fig. S3. SRIM software simulation results.
Fig. S4. Ion beam dosage test.
Fig. S5. Schematic of the bottom layer under elastoplastic deformation.
Fig. S6. Comparison between web-like structures of different topographies after nano-kirigami.
Fig. S7. Origin of the chirality in 3D pinwheel structures.
Fig. S8. Structural designs for optical chirality.
Fig. S9. Numerical calculations and comparison with experiments.
Fig. S10. Extension of nano-kirigami to other platforms.
Movie S1. Nano-kirigami of different structures by programming ion beam irradiation in one step.
Movie S2. Upward and downward buckling with nano-kirigami.
Movie S3. Structural evolution of different web-like structures under nano-kirigami.
Movie S4. Simultaneous upward buckling of an array of pinwheel structures.

REFERENCES AND NOTES

1. G. P. Collins, Science and culture: Kirigami and technology cut a fine figure, together. *Proc. Natl. Acad. Sci. U.S.A.* **113**, 240–241 (2016).
2. S. Perks, Flat-pack physics. *Phys. World* **28**, 21 (2015).
3. J. Rogers, Y. G. Huang, O. G. Schmidt, D. H. Gracias, Origami MEMS and NEMS. *MRS Bull.* **41**, 123–129 (2016).
4. J. Deng, H. Ji, C. Yan, J. Zhang, W. Si, S. Baunack, S. Oswald, Y. Mei, O. G. Schmidt, Naturally rolled-up C/Si/C trilayer nanomembranes as stable anodes for lithium-ion batteries with remarkable cycling performance. *Angew. Chem. Int. Ed.* **52**, 2326–2330 (2013).
5. K. Kuribayashi, K. Tsuchiya, Z. You, D. Tomus, M. Umemoto, T. Ito, M. Sasaki, Self-deployable *origami* stent grafts as a biomedical application of Ni-rich TiNi shape memory alloy foil. *Mater. Sci. Eng. A* **419**, 131–137 (2006).
6. J. L. Silverberg, A. A. Evans, L. McLeod, R. C. Hayward, T. Hull, C. D. Santangelo, I. Cohen, Using origami design principles to fold reprogrammable mechanical metamaterials. *Science* **345**, 647–650 (2014).
7. M. K. Blees, A. W. Barnard, P. A. Rose, S. P. Roberts, K. L. McGill, P. Y. Huang, A. R. Ruyack, J. W. Kevek, B. Kobrin, D. A. Muller, P. L. McEuen, Graphene kirigami. *Nature* **524**, 204–207 (2015).
8. A. Lamoureux, K. Lee, M. Shlian, S. R. Forrest, M. Shtein, Dynamic kirigami structures for integrated solar tracking. *Nat. Commun.* **6**, 8092 (2015).
9. Z. Wang, L. Jing, K. Yao, Y. Yang, B. Zheng, C. M. Soukoulis, H. Chen, Y. Liu, Origami-based reconfigurable metamaterials for tunable chirality. *Adv. Mater.* **29**, 1700412 (2017).

Downloaded from http://advances.sciencemag.org/ on July 6, 2018

10. J. K. Gansel, M. Thiel, M. S. Rill, M. Decker, K. Bade, V. Saile, G. von Freymann, S. Linden, M. Wegener, Gold helix photonic metamaterial as broadband circular polarizer. *Science* **325**, 1513–1515 (2009).
11. M. D. Turner, M. Saba, Q. Zhang, B. P. Cumming, G. E. Schröder-Turk, M. Gu, Miniature chiral beamsplitter based on gyroid photonic crystals. *Nat. Photonics* **7**, 801–805 (2013).
12. N. Liu, H. Guo, L. Fu, S. Kaiser, H. Schweizer, H. Giessen, Three-dimensional photonic metamaterials at optical frequencies. *Nat. Mater.* **7**, 31–37 (2008).
13. A. Rafsanjani, K. Bertoldi, Buckling-induced kirigami. *Phys. Rev. Lett.* **118**, 084301 (2017).
14. Z. Chen, G. Huang, I. Trase, X. Han, Y. Mei, Mechanical self-assembly of a strain-engineered flexible layer: Wrinkling, rolling, and twisting. *Phys. Rev. Appl.* **5**, 017001 (2016).
15. E. A. Peraza-Hernandez, D. J. Hartl, R. J. Malak Jr., D. C. Lagoudas, Origami-inspired active structures: A synthesis and review. *Smart Mater. Struct.* **23**, 094001 (2014).
16. L. Xu, T. C. Shyu, N. A. Kotov, Origami and kirigami nanocomposites. *Acs Nano* **11**, 7587–7599 (2017).
17. Y. Zhang, F. Zhang, Z. Yan, Q. Ma, X. Li, Y. Huang, J. A. Rogers, Printing, folding and assembly methods for forming 3D mesostructures in advanced materials. *Nat. Rev. Mater.* **2**, 17019 (2017).
18. S. Xu, Z. Yan, K.-I. Jang, W. Huang, H. Fu, J. Kim, Z. Wei, M. Flavin, J. McCracken, R. Wang, A. Badea, Y. Liu, D. Xiao, G. Zhou, J. Lee, H. U. Chung, H. Cheng, W. Ren, A. Banks, X. Li, U. Paik, R. G. Nuzzo, Y. Huang, Y. Zhang, J. A. Rogers, Assembly of micro/nanomaterials into complex, three-dimensional architectures by compressive buckling. *Science* **347**, 154–159 (2015).
19. W. J. Arora, S. Sijbrandij, L. Stern, J. Notte, H. I. Smith, G. Barbastathis, Membrane folding by helium ion implantation for three-dimensional device fabrication. *J. Vac. Sci. Technol. B* **25**, 2184 (2007).
20. W. J. Arora, H. I. Smith, G. Barbastathis, Membrane folding by ion implantation induced stress to fabricate three-dimensional nanostructures. *Microelectron. Eng.* **84**, 1454–1458 (2007).
21. A. J. Cui, Z. Liu, J. Li, T. H. Shen, X. Xia, Z. Li, Z. Gong, H. Li, B. Wang, J. Li, H. Yang, W. Li, C. Gu, Directly patterned substrate-free plasmonic "nanograter" structures with unusual Fano resonances. *Light Sci. Appl.* **4**, e308 (2015).
22. T. Buchner, "Kinematics of 3D Folding Structures for Nanostructured Origami™," thesis, Massachusetts Institute of Technology (2003).
23. F. Momeni, N. S. M. M. Hassani, X. Liu, J. Ni, A review of 4D printing. *Mater. Des.* **122**, 42–79 (2017).
24. M. J. Samayoa, M. A. Haque, P. H. Cohen, Focused ion beam irradiation effects on nanoscale freestanding thin films. *J. Micromech. Microeng.* **18**, 095005 (2008).
25. W. D. Nix, B. M. Clemens, Crystallite coalescence: A mechanism for intrinsic tensile stresses in thin films. *J. Mater. Res.* **14**, 3467–3473 (1999).
26. Z. Qin, B. G. Compton, J. A. Lewis, M. J. Buehler, Structural optimization of 3D-printed synthetic spider webs for high strength. *Nat. Commun.* **6**, 7038 (2015).
27. T. Kan, A. Isozaki, N. Kanda, N. Nemoto, K. Konishi, H. Takahashi, M. Kuwata-Gonokami, K. Matsumoto, I. Shimoyama, Enantiomeric switching of chiral metamaterial for terahertz polarization modulation employing vertically deformable MEMS spirals. *Nat. Commun.* **6**, 8422 (2015).
28. R. Zhao, L. Zhang, J. Zhou, T. Koschny, C. M. Soukoulis, Conjugated gammadion chiral metamaterial with uniaxial optical activity and negative refractive index. *Phys. Rev. B* **83**, 035105 (2011).
29. Z. Wang, F. Cheng, T. Winsor, Y. Liu, Optical chiral metamaterials: A review of the fundamentals, fabrication methods and applications. *Nanotechnology* **27**, 412001 (2016).
30. S. P. Rodrigues, S. Lan, L. Kang, Y. Cui, P. W. Panuski, S. Wang, A. M. Urbas, W. Cai, Intensity-dependent modulation of optically active signals in a chiral metamaterial. *Nat. Commun.* **8**, 14602 (2017).
31. M. Hentschel, M. Schäferling, X. Duan, H. Giessen, N. Liu, Chiral plasmonics. *Sci. Adv.* **3**, e1602735 (2017).
32. E. Plum, X.-X. Liu, V. A. Fedotov, Y. Chen, D. P. Tsai, N. I. Zheludev, Metamaterials: Optical activity without chirality. *Phys. Rev. Lett.* **102**, 113902 (2009).
33. S. Zhang, Y.-S. Park, J. Li, X. Lu, W. Zhang, X. Zhang, Negative refractive index in chiral metamaterials. *Phys. Rev. Lett.* **102**, 023901 (2009).
34. J. Kaschke, M. Wegener, Optical and infrared helical metamaterials. *Nanophotonics* **5**, 510–523 (2016).
35. M. Esposito, V. Tasco, M. Cuscunà, F. Todisco, A. Benedetti, I. Tarantini, M. De Giorgi, D. Sanvitto, A. Passaseo, Nanoscale 3D chiral plasmonic helices with circular dichroism at visible frequencies. *ACS Photonics* **2**, 105–114 (2015).
36. A. Y. Zhu, W. T. Chen, A. Zaidi, Y.-W. Huang, M. Khorasaninejad, V. Sanjeev, C.-W. Qiu, F. Capasso, Giant intrinsic chiro-optical activity in planar dielectric nanostructures. *Light Sci. Appl.* **7**, 17158 (2018).
37. C. Li, L. Zhao, Y. Mao, W. Wu, J. Xu, Focused-ion-beam induced Rayleigh-Plateau instability for diversiform suspended nanostructure fabrication. *Sci. Rep.* **5**, 8236 (2015).
38. S. Matsui, T. Kaito, J.-I. Fujita, M. Komuro, K. Kanda, Y. Haruyama, Three-dimensional nanostructure fabrication by focused-ion-beam chemical vapor deposition. *J. Vac. Sci. Technol. B* **18**, 3181–3184 (2000).
39. I. Utke, P. Hoffmann, J. Melngailis, Gas-assisted focused electron beam and ion beam processing and fabrication. *J. Vac. Sci. Technol. B* **26**, 1197–1276 (2008).
40. Z. G. Liu, Z. Liu, J. Li, W. Li, J. Li, C. Gu, Z.-Y. Li, 3D conductive coupling for efficient generation of prominent Fano resonances in metamaterials. *Sci. Rep.* **6**, 27817 (2016).

Acknowledgments: We thank Z. Liu, W. Li, A. Jin, C. Tang, J. Li, and C. Gu from the Laboratory of Microfabrication, Institute of Physics, Chinese Academy of Sciences for assistance in FIB facilities and G. X. Li from Southern University of Science and Technology for useful discussions. **Funding:** This work was supported by the National Key R&D Program of China under grant no. 2017YFA0303800; the National Natural Science Foundation of China under grant nos. 61475186, 61675227, and 11434017; and the visiting program of Chinese Scholarship Council under grant no. 201704910310. N.X.F. and H.D. acknowledge the financial support from Air Force Office of Scientific Research Multidisciplinary Research Program of the University Research Initiative (award FA9550-12-1-0488, "Quantum Metaphotonics and Quantum Metamaterials") and from KAUST-MIT agreement no. 2950 ("Metamaterials by deep subwavelength non-Hermitian engineering"). **Author contributions:** Z.L. and J.L. developed the nano-kirigami methods, fabricated the sample, conducted the optical measurements, and analyzed the data; H.D. and N.X.F performed the mechanical modeling and contributed to the studies on fabrication mechanism, optical chirality, and potential inverse designs; Z.L. performed the numerical simulations on optical chirality; J.L. and Z.-Y.L. conceived the concept of one-step nanofabrication; J.L. and L.L. conceived the concept of nano-kirigami and contributed to the structural designs; and J.L. supervised the whole project. All authors participated in the project discussion and manuscript preparation. **Competing interests:** The authors declare that they have no competing interests. **Data and materials availability:** All data needed to evaluate the conclusions in the paper are present in the paper and/or the Supplementary Materials. Additional data related to this paper may be requested from the authors.

Submitted 27 February 2018
Accepted 29 May 2018
Published 6 July 2018
10.1126/sciadv.aat4436

Citation: Z. Liu, H. Du, J. Li, L. Lu, Z.-Y. Li, N. X. Fang, Nano-kirigami with giant optical chirality. *Sci. Adv.* **4**, eaat4436 (2018).

Downloaded from http://advances.sciencemag.org/ on July 6, 2018

Science Advances
AAAS

advances.sciencemag.org/cgi/content/full/4/7/eaat4436/DC1

Supplementary Materials for

Nano-kirigami with giant optical chirality

Zhiguang Liu, Huifeng Du, Jiafang Li*, Ling Lu, Zhi-Yuan Li*, Nicholas X. Fang*

*Corresponding author. Email: jiafangli@aphy.iphy.ac.cn (J.L.); phzyli@scut.edu.cn (Z.-Y.L.); nicfang@mit.edu (N.X.F.)

Published 6 July 2018, *Sci. Adv.* **4**, eaat4436 (2018)
DOI: 10.1126/sciadv.aat4436

The PDF file includes:

Section S1. Mechanical modeling
Section S2. Optical modeling
Section S3. Extension of nano-kirigami to other materials and geometries
Fig. S1. Illustration of the overhead ion beam blocking and comparison between local and global ion beam irradiation.
Fig. S2. Exotic 3D structures fabricated by nano-kirigami.
Fig. S3. SRIM software simulation results.
Fig. S4. Ion beam dosage test.
Fig. S5. Schematic of the bottom layer under elastoplastic deformation.
Fig. S6. Comparison between web-like structures of different topographies after nano-kirigami.
Fig. S7. Origin of the chirality in 3D pinwheel structures.
Fig. S8. Structural designs for optical chirality.
Fig. S9. Numerical calculations and comparison with experiments.
Fig. S10. Extension of nano-kirigami to other platforms.

Other Supplementary Material for this manuscript includes the following:

(available at advances.sciencemag.org/cgi/content/full/4/7/eaat4436/DC1)

Movie S1 (.avi format). Nano-kirigami of different structures by programming ion beam irradiation in one step.
Movie S2 (.avi format). Upward and downward buckling with nano-kirigami.
Movie S3 (.avi format). Structural evolution of different web-like structures under nano-kirigami.
Movie S4 (.avi format). Simultaneous upward buckling of an array of pinwheel structures.

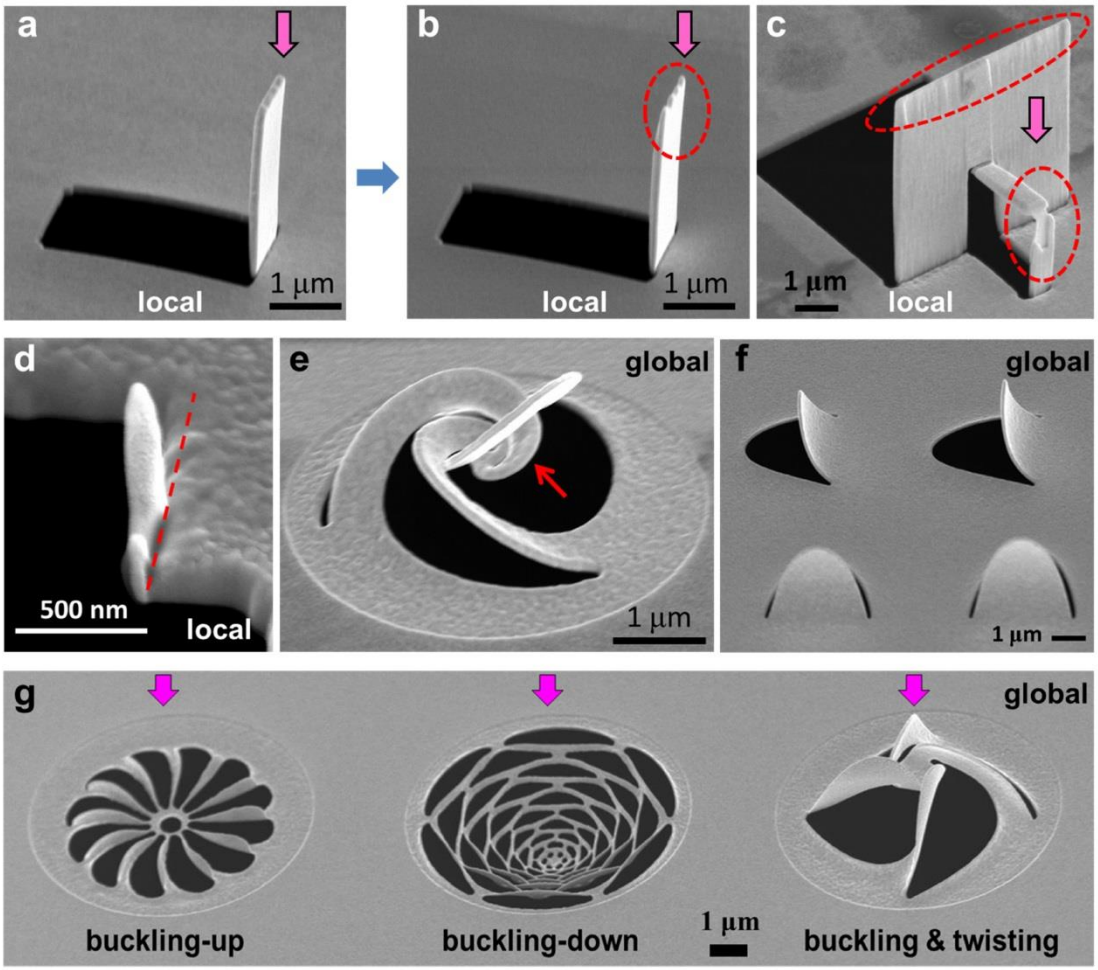

Fig. S1. Illustration of the overhead ion beam blocking and comparison between local and global ion beam irradiation. (**a** to **c**) SEM images of gold micro-stripes fabricated by local irradiation (line-scanning mode) with gallium-based focused ion beam (FIB), which induces zero global curvatures except at the abruptly localized regions (the ion-beam irradiation regions). FIB is incident from the normal direction, as noted by the vertical arrows. When the structures are folded with nearly 90 degrees, the over-head ion beams are partly blocked by the upright structures, which causes the destroys of the structures, as noted by the dashed ellipses in figs. S1b-1c. (**d**) Cross-section SEM image of a upward folded structure after cut by FIB. The dashed line indicates the area where coalescence occurs around the vacancies induced by ion-beam irradiation. (**e**, **f**) SEM images of a twisted triple Fibonacci spirals and tongue-like structures fabricated with global ion-beam irradiation. Non-zero curvatures and cross-over structures (indicated by the red arrow) such as the twisted spirals in (**e**) are impossible to be fabricated with the local irradiation method, reflecting the uniqueness of the global ion-beam irradiation induced nano-kirigami. (**g**) SEM images of a propeller-like structure, a micro-dome and a pinwheel structure fabricated with nano-kirigami in the same gold film, in which the buckling-up, buckling-down and buckling&twisting transformation features are clearly seen. Ion beams are incident from the normal direction (noted by the arrows). Therefore, for the micro-dome structure, this is a buckling-down process when it is seen from the ion-beam illumination direction.

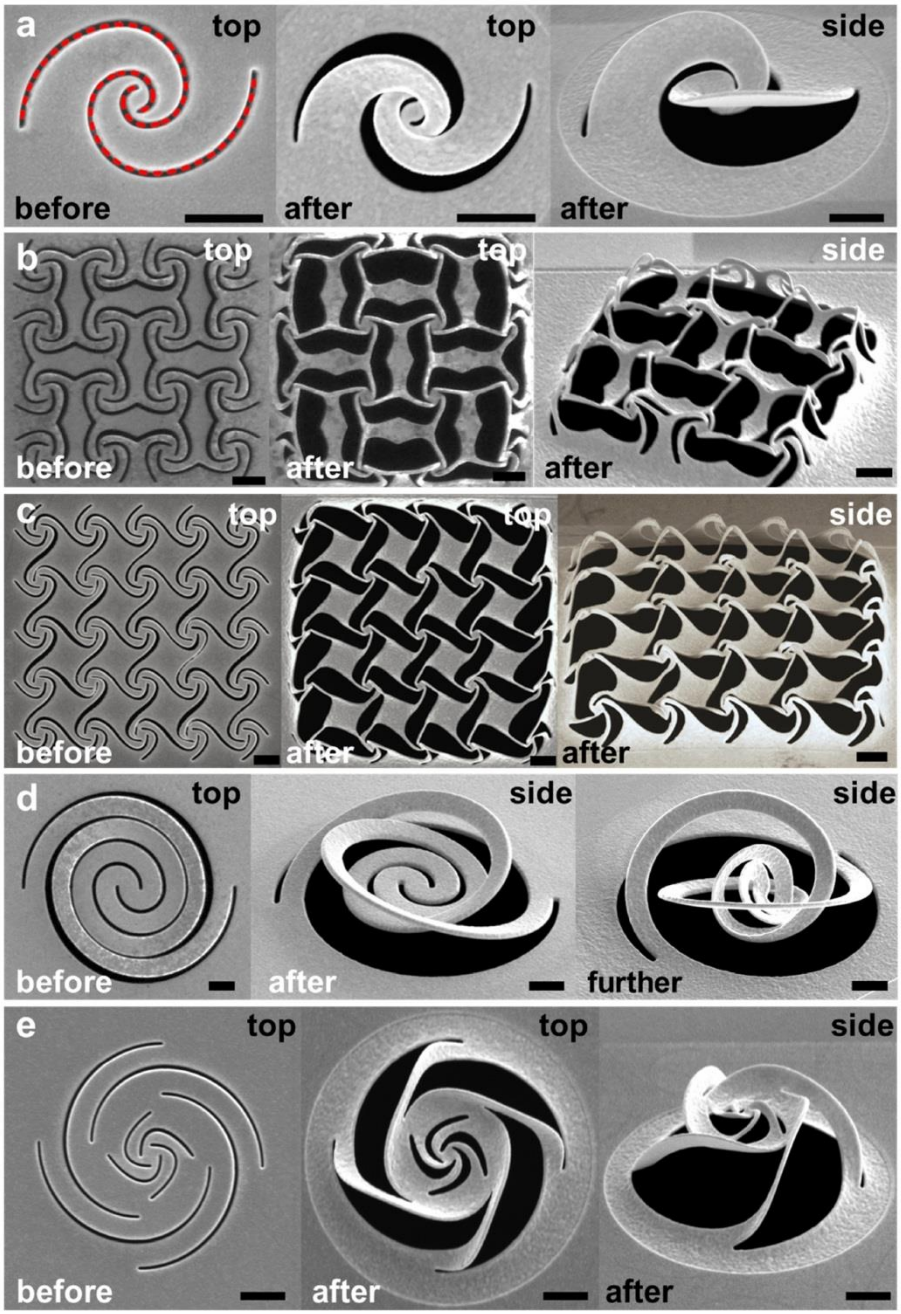

Fig. S2. Exotic 3D structures fabricated by nano-kirigami. Top-view and side-view scanning electron/ion microscope (SEM) images of the typical structures before and after global ion-beam irradiation. (**a**) Combined double Fibonacci spirals. (**b** and **c**) Window-decoration-type interconnected nano-barriers. (**d**) A deformable spiral before and after global ion-beam illumination with different ion doses. (**e**) A combined spiral heterostructure. Scale bars: 1 μm.

Section S1. Mechanical modeling

1.1 The modified bilayer model

Although the effects of focused ion beam (FIB) irradiation on nanoscale thin film have been studied *(19, 24)*, the complete physical mechanisms of how the FIB-induced structural changes are related to material properties and modifications at continuum-mechanics level is still unclear. One reason is that previous theories on membrane folding and unfolding were based on purely elastic material assumptions like Stoney formula *(19, 24)*. They were found inadequate when modeling the constrained film buckling with finite deformation as several key requirements of implementing Stoney formula are not satisfied, including constant radius of curvature and linear elasticity.

We hereby develop a comprehensive mechanics model which characterizes the Au film as a bilayer elastoplastic thin sheet with FIB-induced residual stress gradient, which inherits the bilayer feature of previous models using the well-known Stoney Equation *(24)*, along with explicit forms of distribution of residual stress inside the bilayer and proper justification. This bilayer assumption is well accounted for as the gallium ion implantation depth is found around 20 nm from the top surface and therefore doesn't penetrate the whole Au film in this study, which is predicted by the simulations in fig. S3.

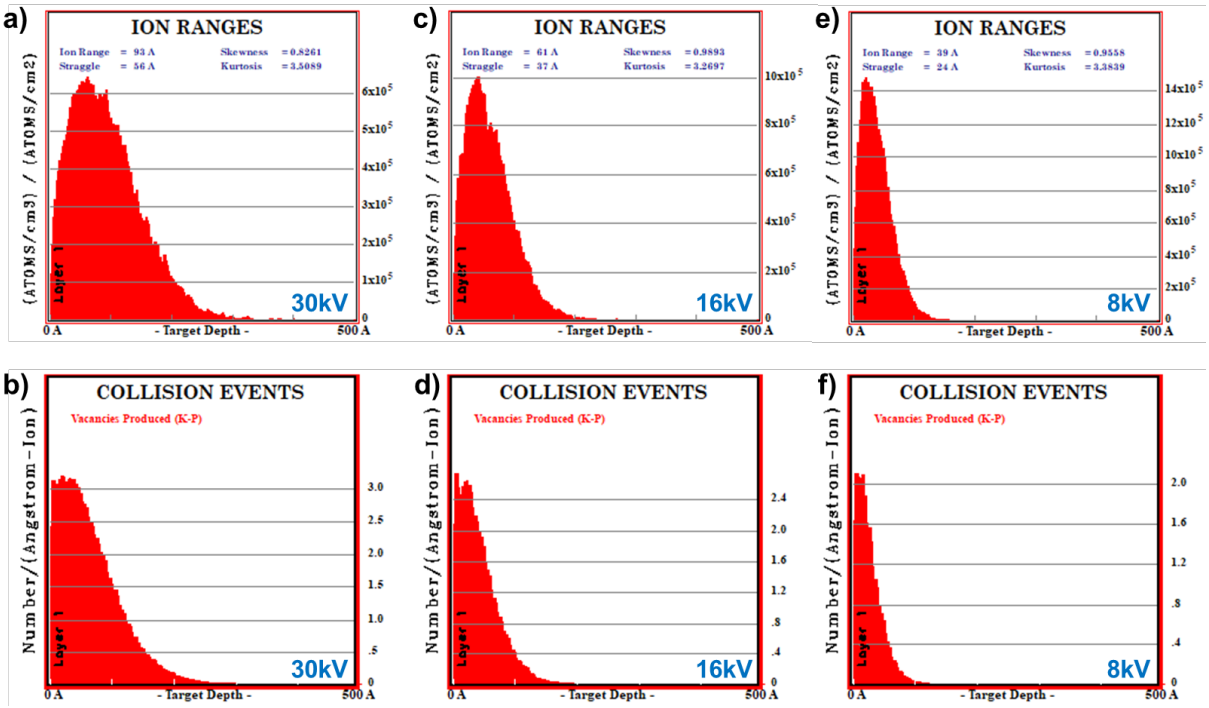

Fig. S3. SRIM software simulation results. SRIM plot of gallium ion concentration and vacancy density as a function of Au film depth under ion beam acceleration voltage of 30, 16 and 8 kV, respectively. The ion range is 9.3, 6.1 and 3.9 nm, respectively, and the penetration depth is less than 20 nm in all cases, both of which decrease with the reduction of acceleration voltage. SRIM software can be available from http://www.srim.org/.

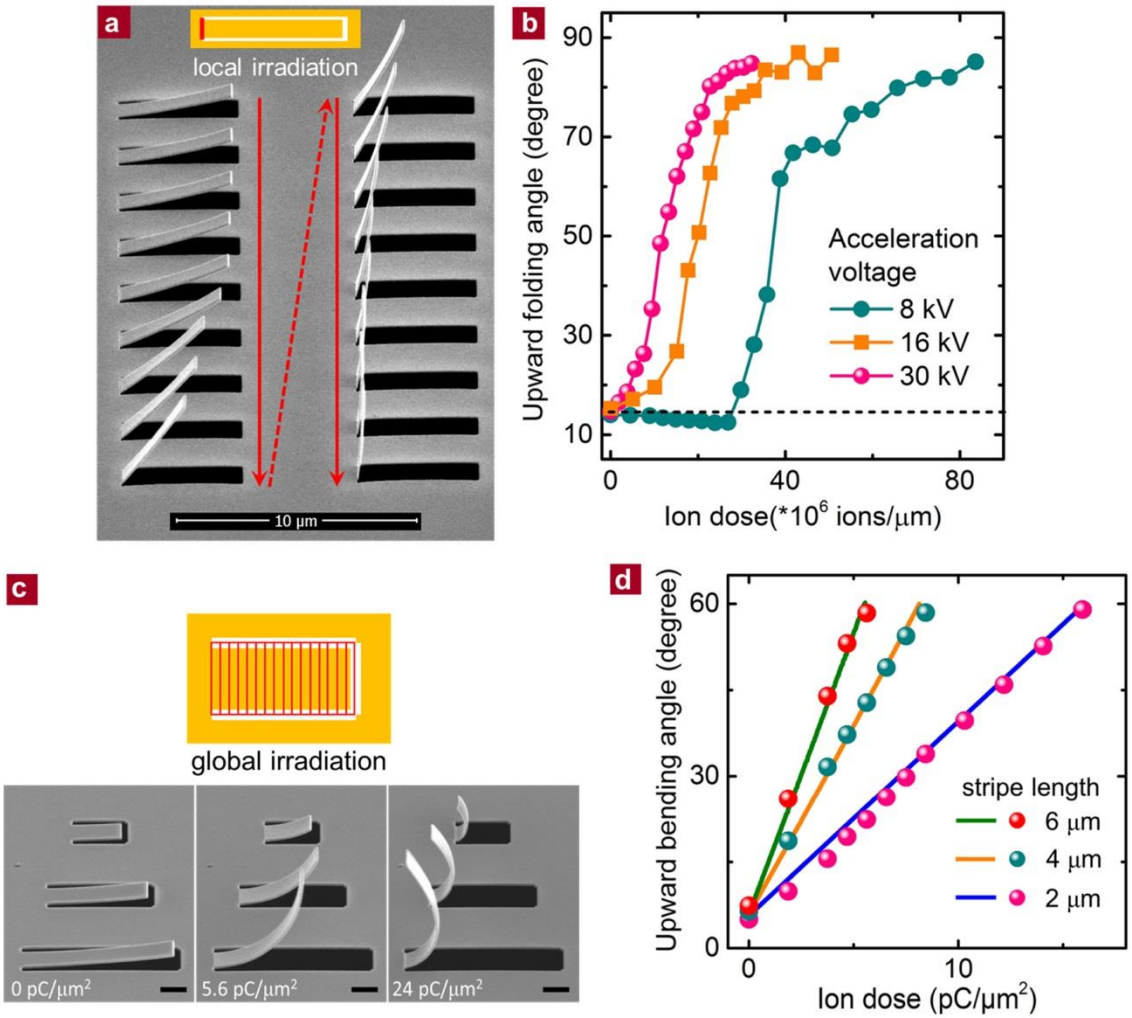

Fig. S4. Ion beam dosage test. (**a**) Side-view SEM images of upward folded micro-stripes (~1 μm×5 μm) after local irradiation (scanning along the red line schematically shown in the inset) with Ga^+ beams with different doses under acceleration voltage of 30 kV. The scanned lines are ~1 μm in length and the linewidth is about 30 nm. The red arrows point out the increasing direction of illumination dosages. (**b**) Measured upward folding angle as a function of ion dose under acceleration voltage of 8, 16 and 30 kV, respectively. It can be seen that Ga^+ implantation induced compressive stress exerts negligible effect in these cases since all of the stripes are upward folded. (**c**) SEM images of the strips under global ion-beam irradiation with increased dose as noted. The lengths of the 1-μm-wide suspended stripes are 6, 4 and 2 μm, respectively. The FIB irradiation areas cover the whole suspended stripe, as the grid area illustrated on the top. Scale bars: 1 μm. (**d**) Measured upward bending angle (solid circles) of micro-stripes as a function of the ion dose under global ion-beam irradiation with acceleration voltage of 30 kV, which agree excellently with the calculations by using our mechanical model (solid lines) under low-dose irradiation. One may notice the warps of the stripes under high-dose irradiation (24 pC/μm^2) in **(c)**, which result in the deviation from calculation due to the decrease of the effective irradiation areas. Nevertheless, at the initial stage and with relatively low-dose irradiation that mostly employed in our nano-kirigami method, the calculations with our mechanical model are well consistent with the experimental results, as plotted in (**d**).

In this model, the most affected top layer of the film undergoes significant changes in crystallographic structures and possible amorphization where motions of dislocations happen at the crystallographic slip planes. The combination of collision-generated vacancies and ion-implantation effects produce tensile-like residual stress throughout the entire scan (fig. S4), and the top amorphous layer subsequently contracts to release the residual stress until new equilibrium is achieved. The irreversible yielding strain associated with

large deformation of folding films in the top layer cannot be neglected, which is evident from the fact that free standing cantilever didn't completely unfold to its initial state after annealing *(19)*. Due to the inelastic nature of deformation in this layer, the residual stress is characterized with an elastic-perfectly plastic model with constant yielding stress as illustrated in Fig. 2a, and a fully plastic zone is expected when the accumulative ion concentration is building up to achieve membrane folding and large global buckling of the 3D structure. The thickness of this amorphous layer is determined by the acceleration voltage and independent of beam current during FIB exposure *(24)*, and this explains why the critical values of ion doses upon which the folding angle of a stripe begins to increase have strong dependence on the acceleration voltages, as verified in fig. S4b.

In comparison, the less affected bottom layer of Au film experiences less amorphization and deforms elastically as the affected top layer contracts due to the tensile residual stress. As the microscopic structures of polycrystalline Au in the bottom layer remain largely intact and ordered than the top layer, a dislocation is less likely to move along crystallographic slip plane and results in higher yield strength of macroscopic material property. Consequently, the stress remains lower than the yielding point and the top-layer contraction induced global bending will generally produce non-uniform stress distribution with constant gradient (i.e. linear form) across the thickness of membrane (detailed justifications will be discussed in next section).

1.2 Distribution of stress in the bottom layer

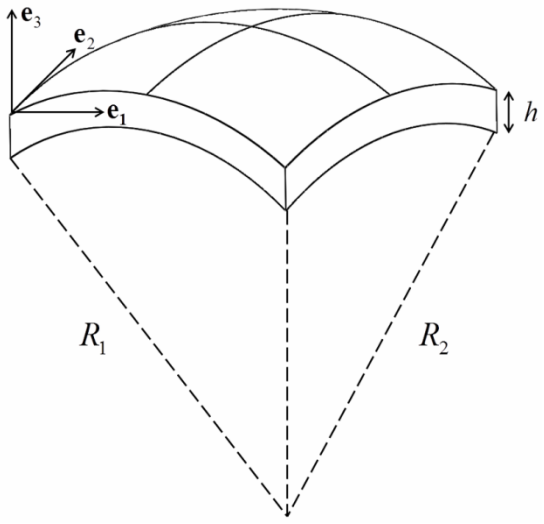

Fig. S5. Schematic of the bottom layer under elastoplastic deformation.

To identify the form of the stress distribution inside the bottom layer under elastoplastic deformation, a schematic of the film is plotted in fig. S5, where the film thickness h in the direction $\mathbf{e_3}$ is much smaller than the characteristic lengths along the other two edges. In such a case, it could essentially be treated as a thin plate with plane stress conditions applied (*21*)

$$\sigma_{\alpha\beta} = \sigma_{\alpha\beta}\left(x_1, x_2\right), \quad \sigma_{33} = \sigma_{13} = \sigma_{23} = 0 \tag{1}$$

where the subscripts α, β range over the values 1 and 2.
For three-dimensional homogeneous, isotropic, linear elastic body, one obtains

$$\varepsilon_{\alpha\beta} = \frac{(1+\nu)}{E}\left(\sigma_{\alpha\beta} - \frac{\nu}{(1+\nu)}(\sigma_{\gamma\gamma})\delta_{\alpha\beta}\right) \tag{2}$$

with $\varepsilon_{13} = \varepsilon_{23} = 0,\ \varepsilon_{33} = -\frac{\nu}{E}\sigma_{\gamma\gamma} = -\frac{\nu}{E}(\sigma_{11} + \sigma_{22})$.

When expressed in terms of strains, the plane stress could be expressed by a constitutive equation

$$\sigma_{\alpha\beta} = \frac{E}{(1+\nu)}\left(\varepsilon_{\alpha\beta} + \frac{\nu}{(1-\nu)}(\varepsilon_{\gamma\gamma})\delta_{\alpha\beta}\right) \tag{3}$$

The radii of curvature (R_1, R_2) in fig. S5 are related with the displacement field $\mathbf{u} = (u_1, u_2, u_3)$ by

$$\frac{1}{R_1} = \frac{u_{3,11}}{\left(1+u_{3,1}^2\right)^{3/2}},\quad \frac{1}{R_2} = \frac{u_{3,22}}{\left(1+u_{3,2}^2\right)^{3/2}} \tag{4}$$

Assuming plane cross-section, the kinematic relationships that relate strains to displacement are expressed as

$$\begin{aligned}
\varepsilon_{11} &= \frac{e}{R_1} - \frac{x_3}{R_1} = (-x_3 + e)\frac{u_{3,11}}{\left(1+u_{3,1}^2\right)^{3/2}} \\
\varepsilon_{22} &= \frac{e}{R_2} - \frac{x_3}{R_2} = (-x_3 + e)\frac{u_{3,22}}{\left(1+u_{3,2}^2\right)^{3/2}} \\
\varepsilon_{33} &= -\frac{\nu}{(1-\nu)}(\varepsilon_{11} + \varepsilon_{22}) = \frac{\nu}{(1-\nu)}(x_3 - e)\left(\frac{u_{3,11}}{\left(1+u_{3,1}^2\right)^{3/2}} + \frac{u_{3,22}}{\left(1+u_{3,2}^2\right)^{3/2}}\right)
\end{aligned} \tag{5}$$

Substituting Eq.(5) back into the constitutive equation Eq.(3), one gets

$$\begin{aligned}
\sigma_{11} &= \frac{E}{1-\nu^2}(-x_3 + e)\left(\frac{u_{3,11}}{\left(1+u_{3,1}^2\right)^{3/2}} + \nu\frac{u_{3,22}}{\left(1+u_{3,2}^2\right)^{3/2}}\right) \\
\sigma_{22} &= \frac{E}{1-\nu^2}(-x_3 + e)\left(\frac{u_{3,22}}{\left(1+u_{3,2}^2\right)^{3/2}} + \nu\frac{u_{3,11}}{\left(1+u_{3,1}^2\right)^{3/2}}\right)
\end{aligned} \tag{6}$$

which is a linear function of the coordinate x_3 along the thickness direction. Therefore, the elastoplastic stress inside the bottom layer keeps a linear distribution across the film thickness.

1.3 Comparison between experimental observations and mechanical modellings

With the above analysis, the ion-beam irradiation induced residual stress within ultra-thin Au film in our modified bilayer model, as illustrated in Fig. 2a, could be simplified as

$$\sigma_{11(22)}^{\text{in-plane}}(x_3)=\begin{cases}\sigma_t=\text{const},\ h_\text{b}<x_3\le h_\text{b}+h_\text{t}\\ \sigma_b=\sigma_0^{\text{in-plane}}+kx_3+o(x_3),\ 0\le x_3\le h_\text{b}\end{cases} \tag{7}$$

Here x_3 is the coordinate in the thickness direction ($\mathbf{e_3}$); h_t and h_b are the thicknesses of top and bottom layers, respectively; σ_t and σ_b are the residual stress in the top and bottom layers, respectively; $\sigma_0^{\text{in-plane}}$ and k are the first-order and second-order coefficient in the asymptotic expansion of stress in the bottom layer with little $o(x_3)$ representing the higher orders (the higher-order term is negligible considering the ultra-small thickness of the films). During the numerical simulations these quantities are treated as fitting parameters when comparing results from computational method with experimental outcomes.

To validate this bilayer model, we first compare the model to experiments with local irradiation induced folding along specific hinge lines (fig. S4a). As shown in fig. S4b, the critical ion dose upon which the upward folding angle of cantilever starts to increase dramatically strongly depends on the acceleration voltage. Although the microscopic physical mechanisms of stress and constitutive relations in the bilayer model differ *(19)*, the curvature of up-folding freestanding film have the same mathematical form if we linearize the radius of curvature expression and assume integral force and momentum freedoms

$$|\kappa|\sim\frac{6(1-\nu)}{E}\sigma^{\text{in-plane, top}}\frac{h_\text{t}(h_\text{t}+h_\text{b})}{h_\text{b}^3} \tag{8}$$

When the ion dose is low, $\sigma_Y^{\text{in-plane, top}}$ doesn't exceed the yield strength of amorphous layer Y_p and the rising stress $\sigma_Y^{\text{in-plane, top}}$ still falls in the elastic regime. At the lowest acceleration voltage tested at 8 kV amorphous top layer is very thin compared with the bottom layer ($\frac{h_\text{t}(h_\text{t}+h_\text{b})}{h_\text{b}^3}\to 0$), hence the curvature $|\kappa|$ remains almost unchanged with increasing stress at low voltage and grows rapidly at higher voltages; after $\sigma_Y^{\text{in-plane, top}}$ reaches the upper bound, the amorphous layer begins to deform plastically with the formation and coalescence of vacancies to initiate the propagation of crack, until the material eventually fails by ductile fracture. New amorphous layer starts to develop on top of previously less affected bottom layer, resulting in decreasing polycrystalline layer thickness h_b and the curvature keeps growing as $\frac{h_\text{t}(h_\text{t}+h_\text{b})}{h_\text{b}^3}$ goes up, which is also validated by experimental observation of localized thinning and necking at the plastic hinges.

To further demonstrate the feasibility of global deformation and quantitatively relate the model parameters to ion irradiation dose, we conduct global ion-beam illumination over the entire freestanding cantilevers (top of fig. S4c) and compare with simulation results. As shown in fig. S4d, when upward bending is initially triggered by ion beam irradiation, the folding angles increase linearly with irradiation dosages and are well predicted by our model in all cases. This excellent agreement between FEM simulation of our model and experiment in determining the bending-dosage relationship within the linear region suggests our bilayer elastoplastic model successfully recover the physical mechanism of residual stress gradients developed during global ion-beam irradiation, which holds great promise in harnessing the rational design of prescribed cut-and-fold patterns on Au nanofilm to actuate global buckling of thin membranes into complex 3D architectures. These advantages have resulted in excellent agreement between numerical simulations and nano-kirigami experiments, such as those in figs. 2b-2e and Fig. 3d of the main text.

1.4 User-defined subroutines in Abaqus software

The deformed configurations of 3D nano-kirigami architectures were calculated with finite element software SIMULIA Abaqus FEA. However, standard SIMULIA Abaqus FEA doesn't allow non-uniform predefined stress fields in Eq. (7) to be specified directly. Alternatively, the non-uniform predefined stress fields could be equivalently represented by giving the structures an effective thermal expansion and a prescribed inhomogeneous initial temperature field. It should be noted that such an equivalent process is only utilized to produce residual stress at the initial step and has no influence over the structure as deformation propagates.

An exemplary Abaqus UTEMP subroutine is shown below, which represents a piece-wise linear temperature field.

```
      SUBROUTINE UTEMP(TEMP,NSECPT,KSTEP,KINC,TIME,NODE,COORDS)
C
      INCLUDE 'ABA_PARAM.INC'
C
      DIMENSION TEMP(NSECPT), TIME(2), COORDS(3)
C

    IF (COORDS(3) .GE. h_b) THEN
          TEMP(1) = T_0
     ELSE

          TEMP(1) = T_1+(T_0-T_1)*(COORDS(3)*k+c)
    END IF

      RETURN
      END
```

Here, h_b stands for the inflection point of stress distribution function (see Fig. 2a for illustration), COORDS(3) indicates the coordinate along the thickness of membrane. T_0 and T_1 are temperature values and can be converted to stress values via thermal expansion coefficients specified in the Abaqus input file. k and c are coefficients for the linear part of this stress distribution.

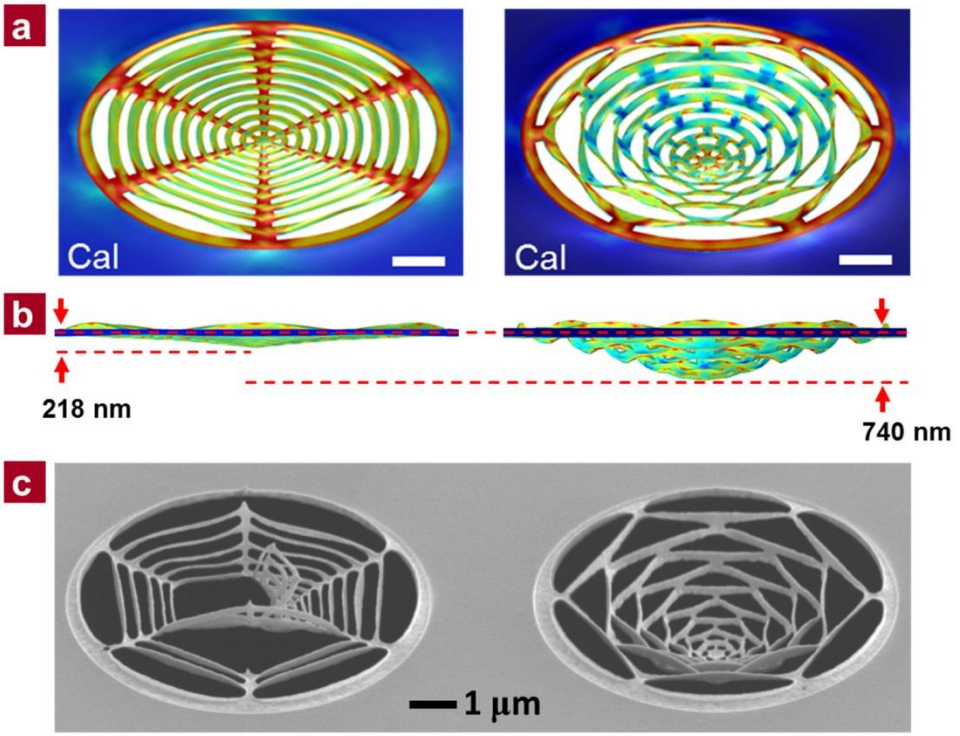

Fig. S6. Comparison between web-like structures of different topographies after nano-kirigami. (**a**) Perspective-view and (**b**) front-view of the calculated results of a spider-web-like and a concentric-arc structure under peak residual stress of 4.5 GPa. Due to their different topographies, the equilibrium stresses are localized at apparently different regions, which result in different downward bending (buckling-down) height as noted in (**b**). It can be seen that the downward buckling of the concentric-arc structure is ~240% larger than that of the spider-web pattern. (**c**) SEM images of a spider-web-like and a concentric-arc structure after the same ion-beam irradiation with relatively large dose. The radial connection in the spider-web structure is broken while the concentric-arc structure is in good shape. This is because in the spider-web structure, the stress is mainly concentrated on the radial connection parts while the concentric-arc structure shows relative uniform stress distribution. Therefore, when the stress increases to certain stage by adding the ion-beam dose, the radial connection parts will firstly receive the fracture threshold. These results are interesting for the structural optimization of nanoscale web-like structure (*26*).

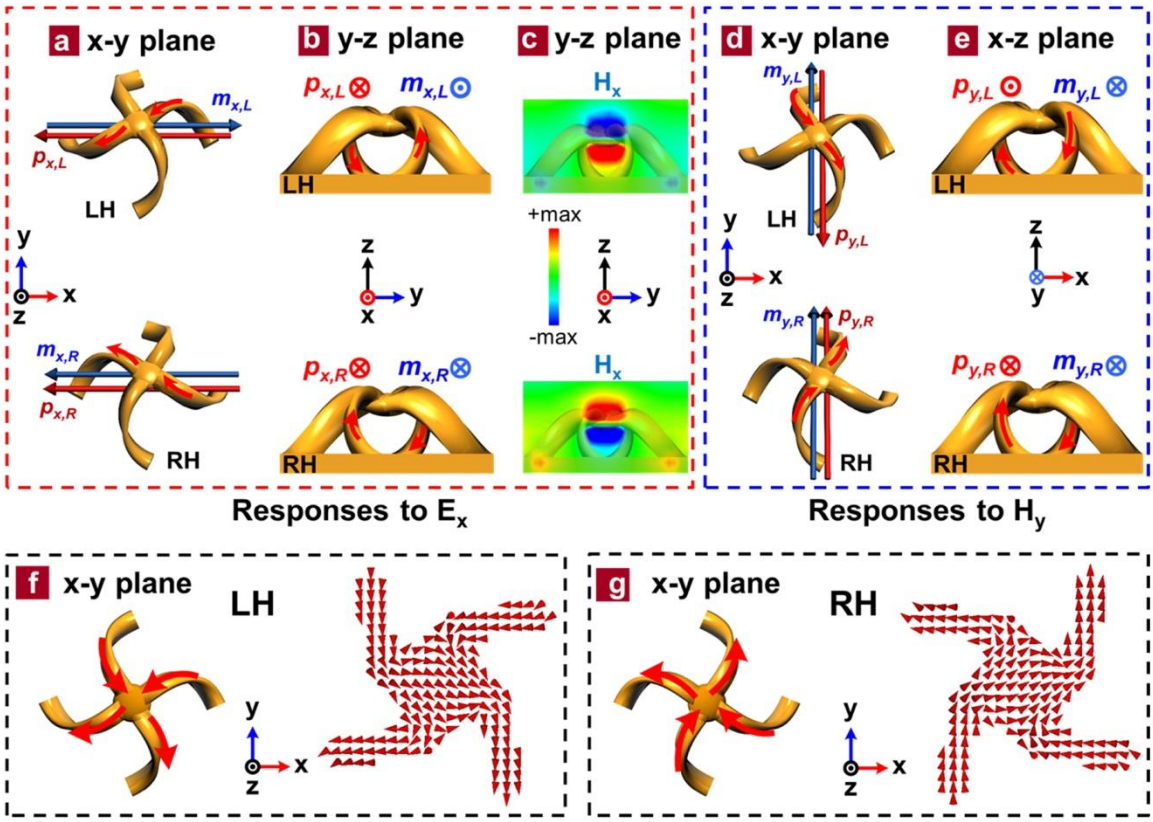

Fig. S7. Origin of the chirality in 3D pinwheel structures. (*9, 28, 31*). (**a** and **b**) Illustration of the responses to the electric field (E_x) of incident light for the left-handed (LH) and right-handed (RH) twisted pinwheels in (**a**) x-y plane and (**b**) y-z plane, respectively. (**c**) Calculated magnetic field (H_x) at wavelength 1.7 μm in the y-z plane (x=0) under x-polarized excitation for a realistic configuration in figs. S9a-9b. The direction of H_x at center part of the pinwheels agrees well with the illustration in (**a**) and (**b**). (**d**, **e**) Illustration of the responses to the magnetic field (H_y) of incident light for LH and RH twisted pinwheels in (**d**) x-y plane and (**e**) x-z plane, respectively. The direction of induced electric moments $p_{i,j}$ ($i = x$ or $y, j = L$ or R) and magnetic moments $m_{i,j}$ at the center parts are noted by the arrows for LH ($j = L$) and RH ($j = R$) pinwheels, respectively. (**f** and **g**) Schematic and calculated electric current density at wavelength 1.7 μm in the center parts of (**f**) LH and (**g**) RH 3D pinwheels, respectively. It can be seen that the calculated current flows are consistent with the illustration in figs. S7a-S7b and figs. S7d-S7e, respectively. It should be mentioned that similar analysis can also be obtained by treating the 3D pinwheel as two cross-linked and twisted Ω-shape circuits (*28*) standing onto a metallic hole array.

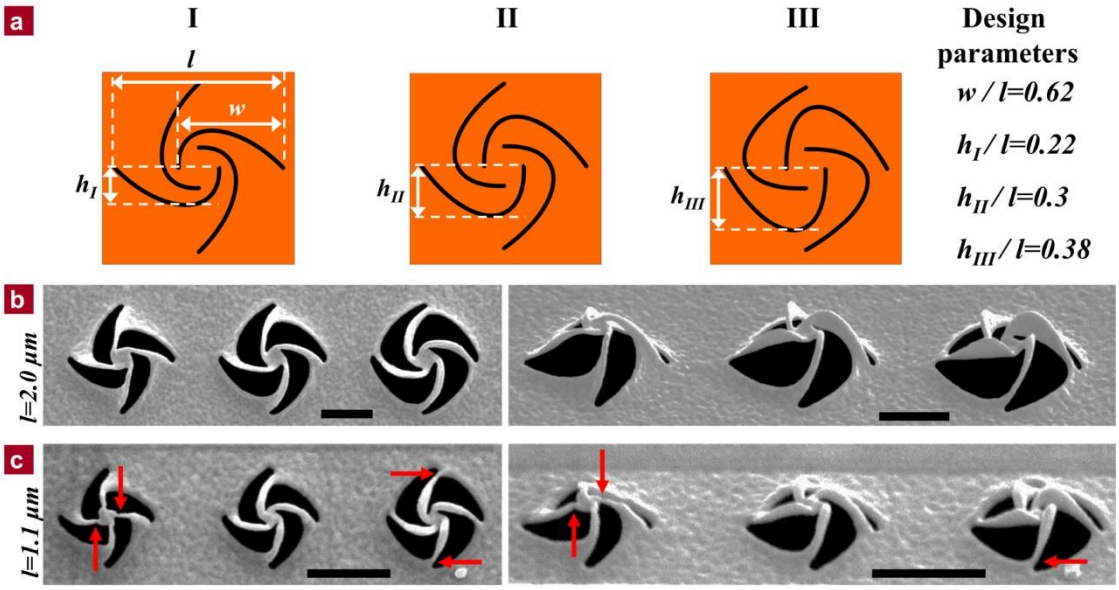

Fig. S8. Structural designs for optical chirality. (**a**) Schematic designs of three types of 2D spiral patterns with different parameters. The curves are varied based on the type I spiral, in which the subunit curve of each arm is defined by a spindle function of $\rho^2 = w^2 sin2\theta$ with $\theta \in [0,\ \pi/4]$. (**b**, **c**) Top-view and side-view SEM images of the 3D pinwheels after global ion-beam irradiation on the 2D spirals with parameters (b) *l*=2 and (c) 1.1 μm, respectively. As noted by the red arrows, the top ends of the arms in type I and the bottom ends of the arms in type III pinwheels are very thin and fragile upon distortion when the structures are scaled down (*l* decreased from 2 μm to 1.1 μm). Scale bars: 1 μm.

Section S2. Optical modeling

The exotic 3D nanostructures enabled by nano-kirigami are complex and irregular in geometries due to their twisting features and atom dislocation process. For example, the 3D pinwheels in Fig. 4b of the main content are involved with twisting in all three dimensions and the structure at small scale *(l*=1.1 μm) does not keep a linear relationship with the large-scale pinwheel (*l*=2 μm in Fig. 3e). This makes it difficult to build a 100% replica model of the real 3D structures, especially at nanoscales. For ease of calculation and analysis, a simplified simulation model is built in fig. S9a-9b according to the SEM images of the structures fig. S9c, which is geometrically similar as that in Figs. 3a of the main text. As a result, the calculated magnetic field and electric current flows (in the center parts of the pinwheels) in fig. S7c, S7f and S7g, as well as the corresponding analysis, are well consistent with the illustration in Figs. 3b-3c of the main text, revealing the physical origin of the optical chirality. Meanwhile, the calculated transmission spectra of the 3D pinwheels are in agreement with the measured results, as shown in figs. S9d-9e. However, due to the minimum transmission caused by the Wood's anomaly at the wavelengths close to the lattice period of 1.45 μm, the retrieved circular dichroism and circular birefringence show unrealistic peaks at this wavelength region, as shown in figs. S9f-9g. These unrealistic data are therefore not shown for clearance in the main text of Figs. 4d-4e.

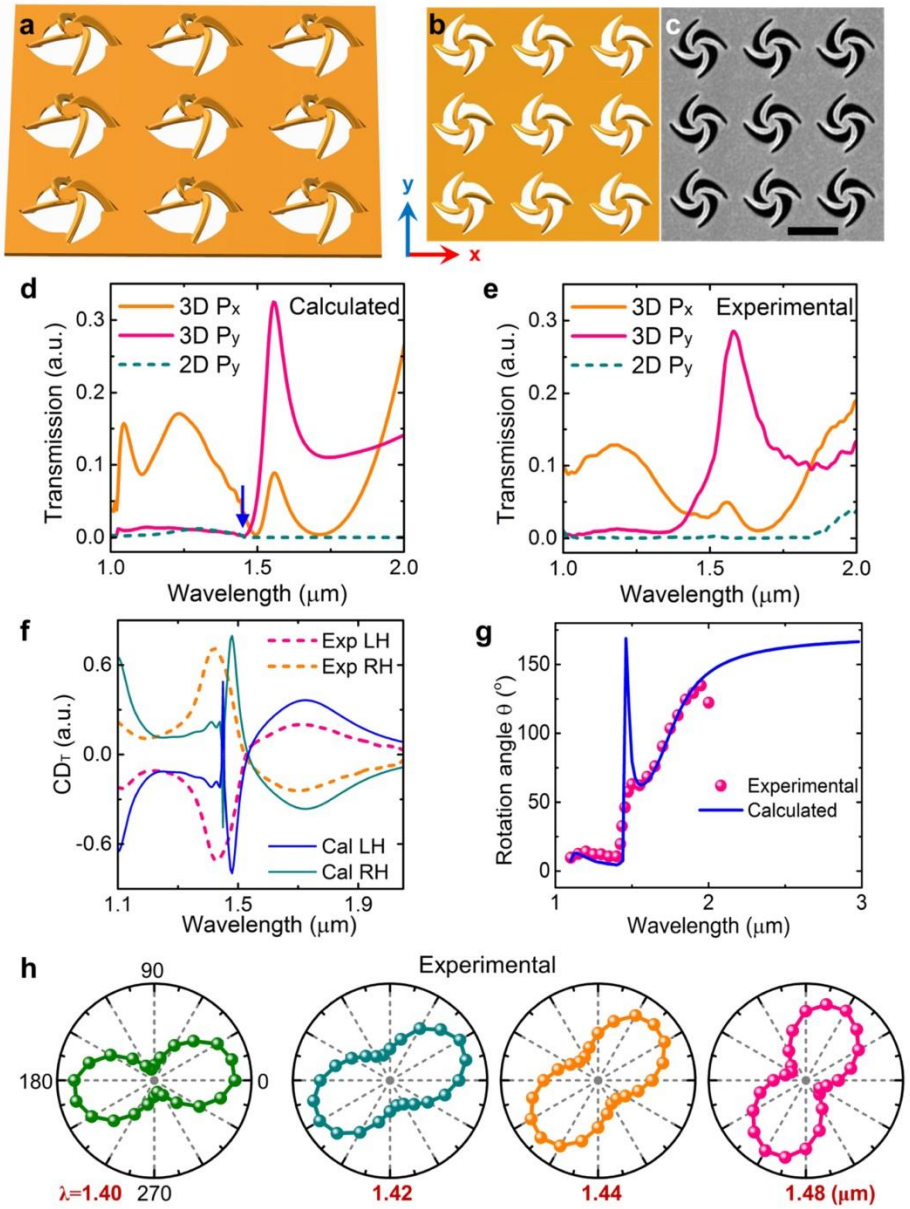

Fig. S9. Numerical calculations and comparison with experiments. (**a** and **b**) Side-view and top-view schematic of the 3D pinwheel in optical modeling, which is quite consistent with the top-view SEM image of the experimental 3D pinwheel in (**c**). (**d**, **e**) Calculated and measured transmission spectra of 3D and 2D pinwheels under detection with x-polarization (P_x) and y-polarization (P_y), respectively. The polarization of incident light is along x-direction. The blue arrow in (**d**) indicates the minimum transmission caused by the Wood's anomaly at the wavelengths close to the lattice period of 1.45 μm. The spectra of LH 3D and 2D pinwheels under y-polarized detection are very different, revealing the tremendous changes brought by the nano-kirigami. (**f**) Experimental (Exp) and calculated (Cal) circular dichroism (CD) in transmission versus wavelength for 3D LH and RH pinwheels, respectively. To elucidate the effects brought by nano-kirigami and to rule out the background influence, here the CD is defined as $CD_T = (T_L - T_R)/(T_L + T_R)$. (**g**) Measured and calculated polarization rotation angle (θ) in anti-clockwise direction versus wavelength for a 3D LH pinwheel structure. Due to the inaccurate retrieve of polarization states at nearly zero transmission at Wood's anomaly, the spectra in (**f**) and (**g**) possess unrealistic sharp peaks around 1.45 μm, which are not shown for clearance in Fig. 4 of the main text. (**h**) Polar-plots of experimental transmission versus detection polarization angle under x-polarized incidence. It can be seen that for wavelengths in the strong CD region (around 1.45 μm), the transmitted light exhibits elliptical polarization states.

Section S3. Extension of nano-kirigami to other materials and geometries

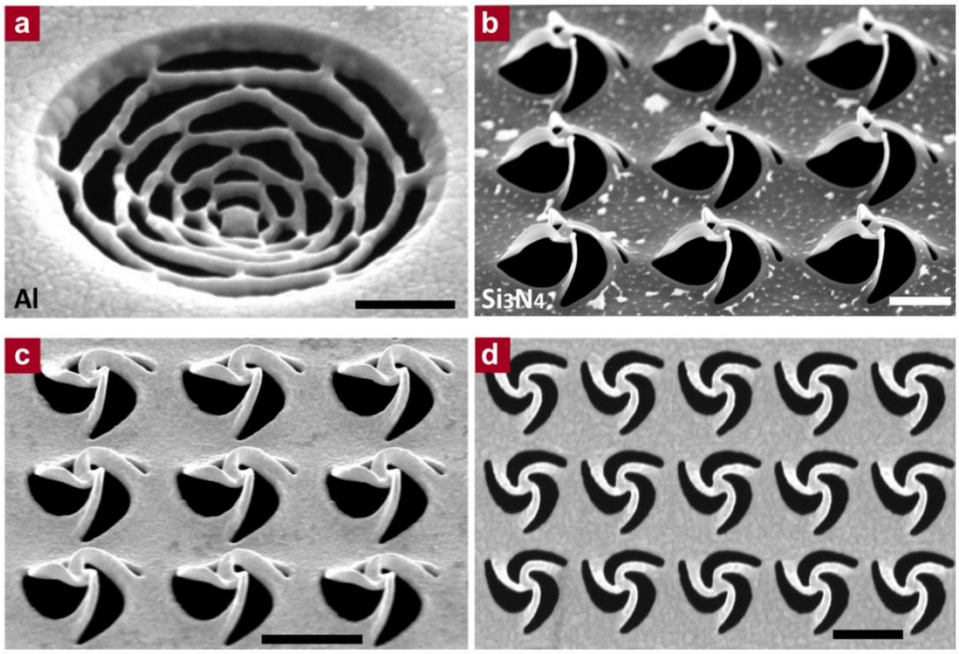

Fig. S10. Extension of nano-kirigami to other platforms. (**a** and **b**) Nano-kirigami enabled 3D structures in (**a**) a 100-nm-thick aluminum film and (**b**) a 50-nm-thick silicon nitride thin film. (**c**) Side-view and (**d**) top-view SEM image of three-arm 3D pinwheels fabricated in a 80-nm-thick gold film. Scale bars: 1 μm.

It should be mentioned that in this paper the residual stress distribution form in Eq. (7) is valid for gold nanofilm under gallium ion irradiation with high acceleration voltage of 30 kV. When using other materials or other types of ion beams, the distribution of vacancies and implanted ions will be different (as could be simulated by SRIM like in fig. S3) and the specific form of the residual stress distribution is therefore upon modifications. Nevertheless, the concept of employing topography-guided stress equilibrium for nano-kirigami is universal, which can be applied to a wide variety of free-standing thin-film materials. For example, a free-standing aluminum thin film with thickness of ~100 nm can be adopted with the topography-guided nano-kirigami (as shown in fig. S10a), although the buckling-up and buckling-down processes are quite different due to the tensile and compressive stresses of aluminum film are distinctive from those of gold (results not shown). In a similar way, commercially available silicon nitride films have also been successfully tested with our nano-kirigami method by initially coating a ultra-thin conductive gold layer, as the result shown in figs. S10b. The geometries of the functional 3D structures by nano-kirigami, as well, could be extended to other types such as a three-arm 3D pinwheel that breaks the center-reversal symmetry (figs. S10c-10d).